JBC ARTICLE

Altered learning, memory, and social behavior in type 1 taste receptor subunit 3 knock-out mice are associated with neuronal dysfunction

Received for publication, December 22, 2016, and in revised form, May 3, 2017 Published, Papers in Press, May 18, 2017, DOI 10.1074/jbc.M116.773820

Bronwen Martin[‡1], Rui Wang[‡1], Wei-Na Cong[‡], Caitlin M. Daimon[‡], Wells W. Wu[‡], Bin Ni[§], Kevin G. Becker[¶], Elin Lehrmann[¶], William H. Wood III[¶], Yongqing Zhang[¶], Harmonie Etienne[‖], Jaana van Gastel[‖**], Abdelkrim Azmi[‖**], Jonathan Janssens[‖**], and Stuart Maudsley[§‖**2]**

*From the [‡]Metabolism Unit, NIA, National Institutes of Health, Baltimore, Maryland 21224, the [§]Receptor Pharmacology Unit, NIA, National Institutes of Health, Baltimore, Maryland 21224, the [¶]Gene Expression and Genomics Unit, NIA, National Institutes of Health, Baltimore, Maryland 21224, the [‖]Translational Neurobiology Group, VIB Department of Molecular Genetics, University of Antwerp, AN-2610 Antwerp, Belgium, and the **Department of Biomedical Sciences, University of Antwerp, AN-2610 Antwerp, Belgium*

Edited by Paul E. Fraser

The type 1 taste receptor member 3 (T1R3) is a G protein-coupled receptor involved in sweet-taste perception. Besides the tongue, the T1R3 receptor is highly expressed in brain areas implicated in cognition, including the hippocampus and cortex. As cognitive decline is often preceded by significant metabolic or endocrinological dysfunctions regulated by the sweet-taste perception system, we hypothesized that a disruption of the sweet-taste perception in the brain could have a key role in the development of cognitive dysfunction. To assess the importance of the sweet-taste receptors in the brain, we conducted transcriptomic and proteomic analyses of cortical and hippocampal tissues isolated from T1R3 knock-out (T1R3KO) mice. The effect of an impaired sweet-taste perception system on cognition functions were examined by analyzing synaptic integrity and performing animal behavior on T1R3KO mice. Although T1R3KO mice did not present a metabolically disrupted phenotype, bioinformatic interpretation of the high-dimensionality data indicated a strong neurodegenerative signature associated with significant alterations in pathways involved in neuritogenesis, dendritic growth, and synaptogenesis. Furthermore, a significantly reduced dendritic spine density was observed in T1R3KO mice together with alterations in learning and memory functions as well as sociability deficits. Taken together our data suggest that the sweet-taste receptor system plays an important neurotrophic role in the extralingual central nervous tissue that underpins synaptic function, memory acquisition, and social behavior.

This work was supported by National Institutes of Health Intramural Research Program Grants AG000915-01 and AG000917-01 from the NIA. This work also was supported by the FWO Odysseus Program and the Flemish Government Inter-university VIND (Flemish Impulse Funding for Networks in Dementia Research) Initiative. The authors declare that they have no conflicts of interest with the contents of this article. The content is solely the responsibility of the authors and does not necessarily represent the official views of the National Institutes of Health.

The raw transcriptomic data have been deposited at Gene Expression Omnibus (GEO)/ArrayExpress under accession number GSE97677.

This article contains supplemental Fig. S1 and Tables S1–S22.

[1] Both authors contributed equally to this work.

[2] To whom correspondence should be addressed: University of Antwerp, VIB Dept. of Molecular Genetics, Universiteitsplein 1, Antwerp 2610. Tel.: 32-3-265-1057; Fax: 32-3-265-1113; E-mail: stuart.maudsley@molgen.vib-ua.be.

The gustatory sweet-taste receptor perception system, although crucial for nutrient sensing along the digestive system, appears more closely interconnected to complex endocrine and neurological functions than thought previously (1–6). The sweet-taste perception process in the tongue, *i.e.* sugar/non-nutritive artificial sweetener gustation, begins with the activation of a heterodimeric G protein-coupled receptor complex, composed of the type 1 taste receptor member 2 (T1R2)[3] and type 1 taste receptor member 3 (T1R3). The T1R2/T1R3 heterodimer facilitates the sensation of a variety of ligands including natural and artificial sweeteners, amino acids, calcium, and sweet-taste proteins (7–13). The T1R3 subunit is widely expressed throughout the brain, with high abundance in the hypothalamus, hippocampus, and cortex (2, 14, 15). Interestingly, the T1R3 receptor possesses a strong structural similarity to the metabotropic glutamate receptors that are crucial for learning, memory, and behavior (16–18). In addition, T1R3 knock-out (T1R3KO) mice demonstrate an inability to respond to monosodium glutamate (8) further supporting the potential importance of this receptor system in regulating neuronal/behavioral activity linked to glutamatergic transmission. Reinforcing a potential synergy between sweet-taste perception and cognitive systems, glucose availability has been strongly associated with effective learning capacity (19–23). Neurometabolic dysfunction is a potent risk factor for multiple neurodegenerative brain diseases (24–29), and alterations in chemosensory (taste/olfaction) perception are common in neurodegenerative diseases and aging (3, 30–36). Specifically, neurodegenerative disorders with strong behavioral phenotypes, such as frontotemporal dementia (FTD) are characterized by alterations in gustation, eating behavior (37–40), glucose metabolism (41, 42), and energetic glucose utilization (43). In our present study,

[3] The abbreviations used are: T1R2, type 1 taste receptor 2; FTD, frontotemporal dementia; ASD, autism spectrum disorder; CA1, cornu ammonis 1; RER, respiratory exchange rate; IPA, ingenuity pathway analysis; NLP, natural language processing; CREB, cAMP response-element-binding protein; NOP, novel object preference; MWM, Morris water maze; AD, Alzheimer's disease; PSD-95, post-synaptic density protein, 95 kDa; L-DOPA, L-3,4-dihydroxyphenylalanine; iTRAQ, isobaric tags for relative and absolute quantification.

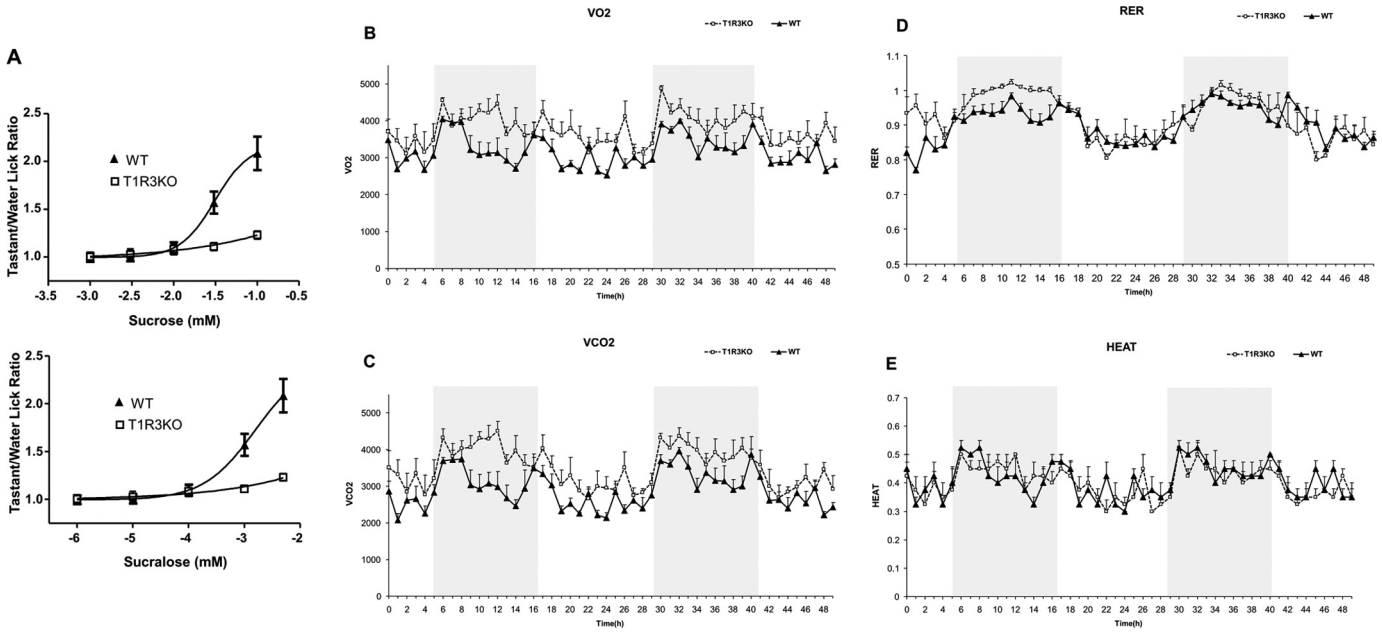

Figure 1. Gustatory and metabolic evaluation of T1R3KO mice compared with WT controls. The ability to perceive the appetitive stimuli, sucrose, and the non-nutritive sweetener, sucralose, was assessed in WT and T1R3KO mice (*A*). T1R3KO mice demonstrated a largely refractory response to the appetitive tastants. Whole-body metabolic status was assessed in T1R3KO mice using a CLAMS (Comprehensive Lab Animal Monitoring System) platform across a variety of outputs (WT, *black triangles*; T1R3KO, *white squares*) including oxygen consumption (VO_2) (*B*), carbon dioxide production (VCO_2) (*C*), Respiratory Exchange Ratio (*RER*–an assessment of the metabolic exchange of oxygen for carbon dioxide) (*D*), and heat production (*E*). Parameters (*B–E*) were measured over a 48-h period. The dark cycle time is indicated by the *gray section* of the pictogram bar in each CLAMS activity. Data are shown as means ± S.E., and $p \leq 0.05$ was considered statistically significant ($n = 8$).

we found that T1R3KO mice demonstrated significant changes in neurosynaptic signaling proteins and structural architecture, altered learning and memory function, and disrupted sociability behavior. These findings demonstrate that an intact T1R2/T1R3 receptor system in the brain is required for effective hippocampal neurotransmissive activity and neuronal architecture.

Results

T1R3 genomic deletion affects taste perception but minimally affects somatic physiology

As part of the core unit of sweet-taste perception (*i.e.* T1R2/T1R3 heterodimer) genomic deletion of the T1R3 receptor is likely to affect this modality. T1R3KO mice demonstrated a significantly blunted ability to respond in an appetitive manner to nutritive (sucrose) or non-nutritive (sucralose) sweet-tasting compounds (Fig. 1*A*). Despite alterations in taste perception we found no significant changes in general feeding behavior or body-weight gain between T1R3KO mice and WT controls. As the expression of T1R2/T1R3 heterodimers is more widespread than thought previously, we investigated the effect of genetic T1R3 disruption upon whole somatic physiology in mice (Fig. 1, *B–E*). Genomic deletion of the T1R3 receptor did not significantly affect oxygen consumption (VO_2), carbon dioxide production (VCO_2), respiratory exchange rate (RER), or heat generation compared with wild-type (WT) controls (Fig. 1, *A–D*). Furthermore, we failed to see any significant differences in ambulatory/vertical activity in the T1R3KO mice (supplemental Fig. S1, *A–C*). We did however find a consistent, but nonsignificant increase in food (Fig. S1*D*) and water (Fig. S1*E*) intake in T1R3KO mice compared with WT controls.

Transcriptomic analysis of central-nervous-system perturbations in T1R3KO mice

From our somatic physiological analyses of the T1R3KO mice (Fig. 1), it was evident that these mice do not present with any significant metabolic issues aside from the altered taste-perception modalities at this experimental age (4–5-months old). Our previous research has demonstrated that systems-wide taste-receptor functionality involves receptor activity not only in the tongue but also in peripheral tissues, *e.g.* pancreas (44), as well as central-nervous-system (CNS) tissues such as the hypothalamus (2). Considering the potential role of the sweet-taste receptor system in neurodegeneration, we next investigated, using differential (between WT and T1R3KO mice) quantitative transcriptomics, the impact of T1R3 deletion upon the integrity of diverse CNS tissues including the cortex (supplemental Table S1), the hippocampus (supplemental Table S2), and the hypothalamus (supplemental Table S3). We had demonstrated previously the applicability of high-dimensionality transcriptomic profiling to generate a holistic appreciation of complex CNS-related functions such as neurodegeneration (45), remedial drug efficacy (46), psychosocial disruption (47), and pathological aging (48). Investigation of the significant differential transcriptomic expression patterns between T1R3KO and WT mice (Fig. 2*A* and supplemental Table S4) demonstrates the presence of multiple transcripts differentially regulated in multiple tissues from T1R3KO mice compared with WT controls, of which the cortex and hippocampus demonstrated the greatest degree of cross-over of T1R3KO-specific altered factors. To validate our transcriptomic data (supplemental Tables S1–S3), we chose five tran-

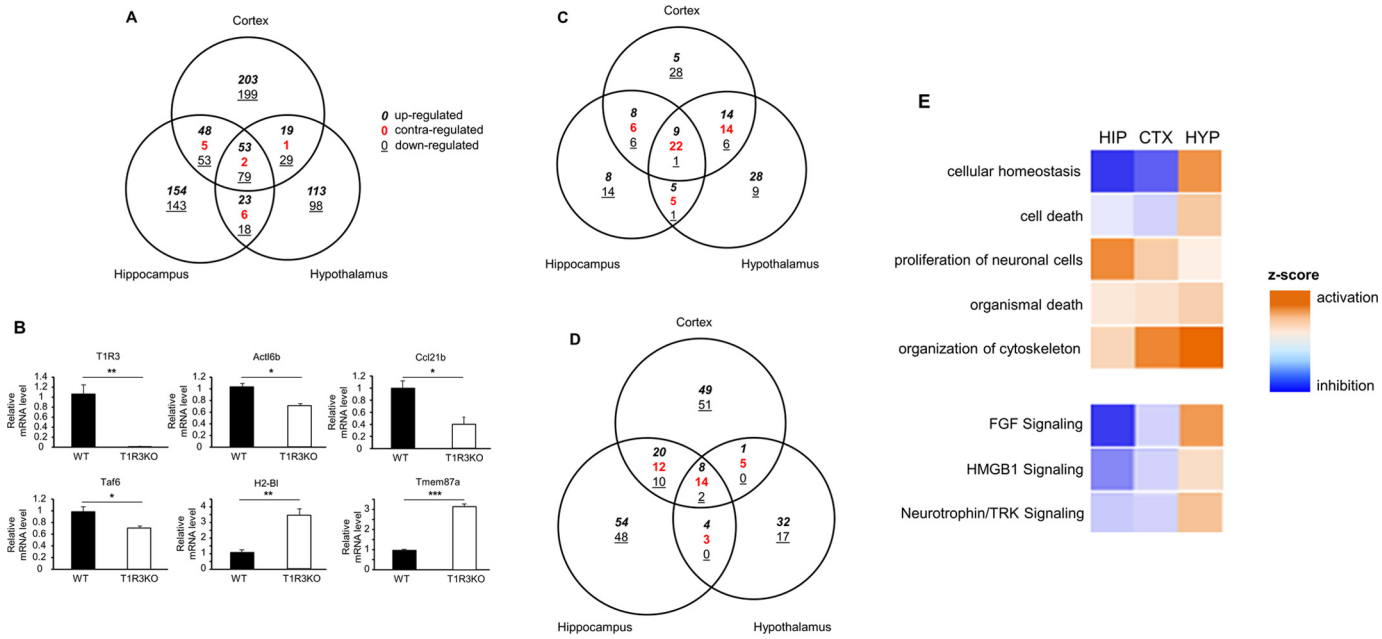

Figure 2. Central nervous system transcriptomic profiling of T1R3KO mice. *A*, Venn diagram analysis of significantly regulated transcripts in the cortex, hippocampus, and hypothalamus of T1R3KO mice compared to WT controls. *B*, PCR validation of randomly selected transcriptomic targets (T1R3, Actl6b, Ccl21b, Taf6, B2-Bl, and Tmem87a: WT, *black bars*; T1R3KO, *white bars*). *C*, Venn diagram analysis of IPA canonical signaling pathway annotation generated using the significantly-regulated cortical, hippocampal, and hypothalamic transcriptomic data as the input. Numerical values for each pathway were generated through calculation (for a specific pathway) of the percent of transcripts up-regulated in the specific pathway minus the percent of the transcripts down-regulated in the specific pathway. *D*, Venn diagram analysis of IPA biofunction/disease annotation data generated using the significantly regulated transcript data from each tissue as the input. Biofunction/disease activating or inhibiting Z-score estimates generated by IPA were employed for this numerical annotation. *E*, heat map illustration of clustered neurodegeneration-related biofunction/disease (*upper panel*) and canonical signaling pathways (*lower panel*: IPA-derived canonical signaling pathway Z-score estimates depicted) from hippocampal (*HIP*), cortical (*CTX*) and hypothalamic (*HYP*) tissues.

scripts from our microarray data, as well as the T1R3 itself, confirming their differential expression in T1R3KO mice compared with WT controls by using quantitative real-time PCR (Fig. 2*B*). We confirmed our array data (supplemental Tables S1–S3) indicating a T1R3KO-dependent decrease in Actl6b (actin-like 6B), Ccl21b (chemokine (C-C motif) ligand 21B (leucine)), and Taf6 (TAF6 RNA polymerase II, TATA-box-binding protein (TBP)-associated factor), along with a T1R3KO-dependent potentiation of H2-Bl (histocompatibility 2, blastocyst) and Tmem87a (transmembrane protein 87A) transcript expression (Fig. 2*B*). Comparing transcriptomic differences between T1R3KO and WT mice, it is clear that considerable significant differences are present, *e.g.* 691 cortical transcripts, 584 hippocampal transcripts, and 441 hypothalamic transcripts. We employed signaling pathway analysis to elucidate the signaling activities that were potentially perturbed in T1R3KO mice. Using ingenuity pathway analysis (IPA), we investigated how the distinct transcriptomic states of the T1R3KO mouse cortex, hippocampus, or hypothalamus translated into potential canonical signaling or biofunction/disease pathways (supplemental Tables S5 (cortex), S6 (hippocampus), and S7 (hypothalamus) and Fig. 2*C*). With respect to the IPA canonical signaling pathway analysis, it was evident that the hypothalamus was effectively dominated by "up-regulated" pathways (comprising a predominance of up-regulated related transcripts). The cortex and the hippocampus demonstrated only a small number of up-regulated pathways. Conversely, both the cortex and the hippocampal tissues were dominated by a large number of "down-regulated" pathways (comprising a predominance of down-regulated related transcripts), whereas the hypothalamus possessed the inverse, *i.e.* only a small number of down-regulated pathways. As with our canonical signaling pathway analysis, we found a stronger commonality of predicted T1R3KO-related IPA biofunctions between cortical and hippocampal tissues compared with hypothalamic tissues (Fig. 2*D*). To further investigate the divergence between the hippocampal/cortical tissues and the hypothalamus, we generated a heat map of both the canonical signaling pathways and the biofunction pathways correlating to neurophysiological parameters linked to cognitive function and behavior (Fig. 2*E* and supplemental Tables S8 (cortex), S9 (hippocampus), and S10 (hypothalamus)). For many of the important neurophysiological functionalities indicated in Fig. 2*E*, the associated Z-scores again demonstrated a tighter functional grouping between the cortex and hippocampus compared with the hypothalamus. Pathway annotation of the cortical and hippocampal data demonstrated multiple pro-neurodegenerative activities, *e.g.* reductions in cellular homeostasis and neurotrophin receptor signaling. The hippocampal data set demonstrated some of the strongest neurodegenerative activity (IPA signaling pathway and biofuntions) predictions, in terms both of up- and down-regulation, among the three tissues. Hence, hippocampal tissues demonstrated the lowest Z-scores for cellular homeostasis, organismal death, organization of cytoskeleton, FGF signaling, HMGB1 signaling, and neurotrophin/TRK signaling and the highest Z-score for proliferation of neuronal cells. In light of these predictive functional signaling divergences and differential transcriptomic data, we next chose to investigate the actual proteomic differences between T1R3KO and the WT controls in the most closely, functionally clustered tissues that

Table 1

Top 10 most upregulated or downregulated proteins in T1R3KO murine hippocampus *versus* WT control hippocampus

For each significantly identified protein the official Gene Symbol, protein description, Log_2 iTRAQ expression ratio (T1R3KO *vs.* WT control), and molecular functionality are given. Proteins denoted in red were significantly elevated in T1R3KO *vs.* WT and those in green significantly downregulated in T1R3KO *vs.* WT controls.

Gene Symbol	Protein Description	Log_2 iTRAQ ratio	Molecular Function
Cadm3	Cell adhesion molecule 3	1.060526336	Brain specific, calcium-independent cell adhesion molecule
Uchl5	Ubiquitin carboxyl-terminal hydrolase isozyme L5	1.051728731	Proteasomal cysteine deubiquitinase
Slc8a1	Sodium/calcium exchanger 1	1.039097993	Sodium calcium exchanger
Fam92b	Protein FAM92B	1.01090024	Ileal Crohns disease
Rps19	40S ribosomal protein S19	0.987158528	FGF and RNA binding
Fbxo2	F-box only protein 2	0.900195816	Endoplasmic reticulum-associated degradation pathway
Pin1	Peptidyl-prolyl cis-trans isomerase NIMA-interacting 1	0.832141687	Stress response, neuronal differentiation and survival
Ppp2ca	Serine/threonine-protein phosphatase 2A catalytic subunit alpha isoform	0.818459445	Microtubule and Raf regulation - cell growth and division
Mpst	3-mercaptopyruvate sulfurtransferase	0.801215378	Regulation of hydrogen sulphide production
Acly	ATP-citrate synthase	0.795662875	Synthesis of cytosolic Acetyl-CoA
Hint1	Histidine triad nucleotide-binding protein 1	-0.794455526	Regulator of p53 apoptosis/DNA damage
Trim2	Tripartite motif-containing protein 2	-0.848578698	Regulator of neuronal ischemic tolerance
Cyb5a	Cytochrome b5	-0.858707624	Electron carrier for membrane bound oxygenases
Cisd1	CDGSH iron-sulfur domain-containing protein 1	-0.878522177	Fe-S cluster shuttling and/or in redox reactions
Inpp4a	Type I inositol-3,4-bisphosphate 4-phosphatase	-0.935804513	Regulates cell growth and proliferation
Txlng	Gamma-taxilin	-0.942858786	Inhibits ATF4-mediated transcription - cell cycle control
Ppp2r2a	Serine/threonine-protein phosphatase 2A 55 kDa regulatory subunit B alpha isoform	-0.954919786	Cell cycle regulation - phosphatase scaffolding
Phb2	Prohibitin-2	-0.982419879	Mitochondrial respiration activity in aging
Stxbp5	Syntaxin-binding protein 5	-0.999837848	Synaptic transmission and glucose transport
Gpr143	G-protein coupled receptor 143	-1.675131451	DOPA receptor - β-arrestin regulator

Table 2

Top 10 most upregulated or downregulated proteins in T1R3KO murine cortex *versus* WT control cortex

For each significantly identified protein the official Gene Symbol, protein description, Log2 iTRAQ expression ratio (T1R3KO *vs.* WT control), and molecular functionality are given. Proteins denoted in green were significantly elevated in T1R3KO *vs.* WT and those in green significantly downregulated in T1R3KO *vs.* WT controls.

Gene Symbol	Protein Description	Log2 iTRAQ ratio	Molecular Function
Nrxn1	Neurexin-1-alpha	1.626226549	Neuronal cell adhesion receptor
Sbf1	Myotubularin-related protein 5	1.622829104	Protein tyrosine phosphatase
Cct8	T-complex protein 1 subunit theta	1.418418445	Controls protein folding upon ATP hydrolysis
Cers4	Ceramide synthase 4	1.386286476	Production of sphingolipids
Psmb5	Proteasome subunit beta type-5	1.381218148	Proteasomal regulation of Nrf2-ARE pathway
Gabpa	GA-binding protein alpha chain	1.380516613	DNA and chromatin binding
Nptxr	Neuronal pentraxin receptor	1.369249415	Synaptic remodelling
Rab12	Ras-related protein Rab-12	1.286291236	Membrane trafficking/vesicle fusion
Ahsa1	Activator of 90 kDa heat shock protein ATPase homolog 1	1.257027045	HSP90 ATPase activity regulation
Pip5k1c	Phosphatidylinositol-4-phosphate 5-kinase type-1 gamma	1.237180188	Clathrin-coated pit assembly regulation
Cacna2d1	Voltage-dependent calcium channel subunit alpha-2/delta-1	-0.587241948	Regulator of calcium channel activity
Adssl1	Adenylosuccinate synthetase isozyme 1	-0.593517907	Purine nucleotide conversion
Rps11	40S ribosomal protein S11	-0.613996614	Ribosomal RNA binding
Nudt3	Diphosphoinositol polyphosphate phosphohydrolase 1	-0.639043955	Negative regulation of ERK pathway
Ogt	UDP-N-acetylglucosamine--peptide N-acetylglucosaminyltransferase 110 kDa subunit	-0.650875526	Regulation of insulin resistance
Pdxp	Pyridoxal phosphate phosphatase	-0.740961259	Regulation of cytoskeletal activity
Kcnab2	Voltage-gated potassium channel subunit beta-2	-0.746651928	Control of neural excitability
Actbl2	Beta-actin-like protein 2	-0.746787953	Cell motility
Isoc2a	Isochorismatase domain-containing protein 2A, mitochondrial	-0.830766988	Interaction with p16(INK4a)
Nckipsd	NCK-interacting protein with SH3 domain	-0.923547803	Actin polymerization

are strongly linked to neurodegenerative processes, *i.e.* the hippocampus and cortex.

Proteomic expression profile of T1R3KO hippocampal and cortical tissues

Using iTRAQ-based proteomics we assessed the high-dimensionality protein expression profiles of T1R3KO mice compared with WT controls. The top 10 significantly up- and down-regulated proteins in the hippocampus and the cortex are organized in Tables 1 and 2 respectively. The following general trend is apparent, *i.e.* neuroprotection systems are down-regulated, whereas the cell growth and cell division systems are up-regulated. We identified 21 proteins significantly up-regulated and 28 proteins significantly down-regulated in the T1R3KO hippocampus compared with the WT controls (Fig. 3*A* and supplemental Table S11, $p < 0.05$).

To validate our iTRAQ data, we selected three proteins and verified their predicted expression profile using Western blotting (Fig. 3*B*). For all selected proteins (Cplx1, complexin 1; Hint1, histidine-triad nucleotide-binding protein 1; and Slc8a1, solute carrier family 8 (sodium/calcium exchanger), member 1) our Western blot analysis confirmed the mass spectrometry

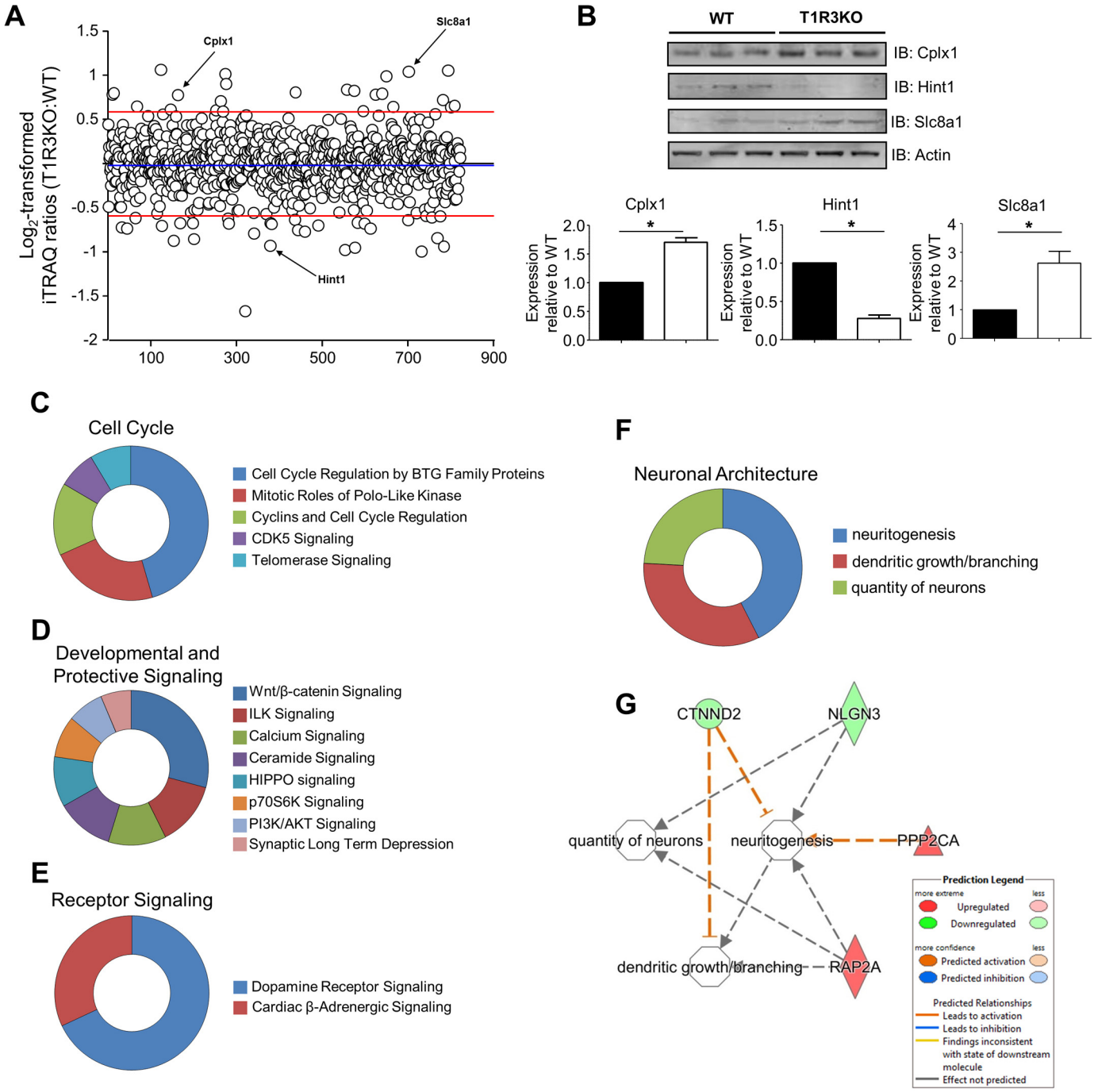

Figure 3. Differential proteomic expression patterns in T1R3KO hippocampus *versus* WT controls iTRAQ data. *A*, $\log_2$-transformed ratios (T1R3KO:WT) from hippocampal iTRAQ data are displayed; proteins with significantly differential expression ($p \leq 0.05$) in T1R3KO *versus* WT control are above or below the *red lines* ($n = 3$ mice/genotype). *B*, Western blot validation of randomly selected proteins differentially expressed in the T1R3KO hippocampus. The iTRAQ-generated expression profiles of Cplx1, Hint1, and Slc8a1 were all confirmed by Western blotting of T1R3KO and WT mice. Additionally actin-normalized protein expression levels are shown. *Error bars* represent mean ± S.E.; $p \leq 0.05$ was considered statistically significant. *C–E*, pie charts depicting the distribution of the canonical signaling pathway groups identified in the T1R3KO data set using IPA according to specific biological functions, *i.e.* cell cycle (*C*), developmental and protective signaling (*D*), and receptor signaling (*E*). *F*, pie chart identifying the multiple biofunction/disease pathway annotations of the significant proteomic data. *G*, using IPA-based protein signaling network generation, the most coherent interactions responsible for the associated T1R3KO biofunctions/diseases (represented in *F*) are highlighted.

data (supplemental Table S11). Compared with the transcriptomics, which indicates functional intent, the verification of actual protein-expression profiles likely represents a more proximal mechanism by which to elucidate the differences in cell-signaling activity between T1R3KO and WT mice. Using our proteomics data along with a multidimensional informatics approach, we next investigated the distinct signaling patterns intrinsic to T1R3KO mice. Applying IPA canonical signaling pathway analysis (with an IPA hippocampal-specific background-reference data set) to the significant hippocampal proteomic data, we found that multiple pathways linked to cell cycle control (CDK5 signaling, telomerase signaling), develop-

mental/neuroprotective activity (Wnt/β-catenin signaling, synaptic long-term depression), and receptor signaling (dopamine-receptor signaling and β-adrenergic signaling) were significantly enriched (Fig. 3, *C–E*, and supplemental Table S12). We also interrogated this proteomic data set for potential IPA biofunction/disease activity (Fig. 3, *F* and *G*, and supplemental Table S13). We found that there was a strong data-set enrichment for proteins associated with neuronal architecture and remodeling (neuritogenesis, dendritic growth/branching, quantity of neurons) (Fig. 3, *F* and *G*, and supplemental Table S13). Using IPA-based network analysis between these significantly enriched IPA biofunction pathways, it was clear that these activities were likely related to one another and coordinated via multiple interacting proteins identified using iTRAQ (Ctnnd2, catenin δ2; Nlgn3, neuroligin 3; Ppp2ca, serine/threonine-protein phosphatase 2A catalytic subunit α; Rap2a, Ras-related protein Rap-2a (Fig. 3*G*)).

As with the T1R3KO hippocampus, we were able to identify multiple significantly regulated ($p < 0.05$) proteins (45 up-regulated and 10 down-regulated, Fig. 4*A* and supplemental Table S14) in the T1R3KO cortex compared with WT controls. We chose three exemplary proteins (Rps11, ribosomal protein s11; Hint1, histidine triad nucleotide-binding protein 1; and Itsn1, intersectin 1) that were significantly and differentially regulated between T1R3KO and WT mice to verify our proteomic data set (Fig. 4*B*). We also examined, at the signaling pathway level (Fig. 4, *C–G*, and supplemental Table S15) and the biofunction level (Fig. 4, *H* and *I*, and supplemental Table S16), the physiological nature of the cortex T1R3KO proteomic data. Using canonical signaling pathway analysis, a strong neurosynaptic functional signature was generated by the cortex T1R3KO data set, *i.e.* multiple signaling pathways clustered around functions such as cell-cycle control (EIF2 signaling and Cdk5 signaling), developmental signaling (mTOR signaling and ceramide signaling), receptor signaling (ephrin-receptor signaling and HMGB1 signaling), cytoskeletal regulation (RhoA signaling and RhoGDI signaling), and vesicular endocytosis (caveolar-mediated endocytosis signaling and macropinocytosis signaling).

Reinforcing this unbiased proteomic interpretation, we also found that with cortical data-set annotation using biofunction analysis (supplemental Table S16) a strong enrichment of activity functions linked with neuronal architecture modification was evident (Fig. 4, *H* and *I*). From this biofunction analysis a focused network of interactions between Nrxn1 (neurexin 1), Ezr (ezrin), Grin2a (glutamate receptor ionotropic, NMDA 2A), RhoA (Ras homolog gene family, member A), Ptpra (receptor-type tyrosine-protein phosphatase α), Itsn1 (intersectin 1), Syncrip (synaptotagmin-binding, cytoplasmic RNA-interacting protein), Dnm3 (dynamin 3), and Pip5k1c (phosphatidylinositol-4-phosphate 5-kinase type-1 γ) likely occurs to control/modulate neuronal architecture in the context of cortical T1R3 loss.

Natural language-based informatics investigation of T1R3KO-specific proteomic disruption

To obtain a more data-specific appreciation of our proteomic data sets, we employed a biomedically focused natural language processing (NLP) informatics interpretation approach (49) using the *Textrous!* program (50). Using the individual processing mode of *Textrous!* to interrogate the significantly regulated hippocampal proteomic data-set, we extracted and correlated to the input data-set proteins multiple biomedically relevant words that clustered into several functional categories (Fig. 5, *A* (neuronal), *B* (synapse), *C* (vesicular trafficking), *D* (neurotransmission), *E* (Disease-related), and *F* (cytoskeleton)). Based on these functional *Textrous!* clusters, we generated a cumulative expression score for the proteins in these groups to indicate a general trend for the expression pattern (*i.e.* T1R3KO *versus* WT) of proteins associated with these semantically associated terms (Fig. 5*G*). Using this methodology we found that the "neuronal," "synapse," "neurotransmission," and "disease-related" clusters presented a profound trend for down-regulation (calculated using both the mean or sum of the $\log_2$ expression ratio scores for the proteins linked to these functions (supplemental Table S17), whereas only "vesicular trafficking" and "cytoskeleton" were populated by generally up-regulated proteins (Fig. 5*G* and supplemental Table S17).

Performing analogous *Textrous!*-based analysis of the cortical proteomic data set for T1R3KO mice, we found that the significantly regulated proteins clustered into two main groups, cytoskeleton and monomeric G proteins (Fig. 6, *A* and *B*). For both of these clusters all of the proteins linked to these *Textrous*!-extracted functions were largely overexpressed in T1R3KO mice compared with WT-control cortices (Fig. 6*C* and supplemental Table S18). Compared with standard pathway annotation processes that use curated language-based interpretation (*e.g.* KEGG pathways) the *Textrous!* program is able to extract more experiment-specific data-descriptive noun phrases linked to the input proteins (50).

Therefore to reinforce our observed distinctions between NLP-based analyses of hippocampal and cortical data sets, we also used these semantically associated noun phrases linked to the hippocampal (supplemental Table S19) or cortical (supplemental Table S20) proteomic data sets as the input to generate complex and highly nuanced word clouds that represent a more gestalt-type interpretation of the proteomic data (Figs. 7*A* (hippocampus) and 8*A* (cortex)). The use of free-form quantitative word clouds to convey complex noncanonical signaling-activity relationships is becoming more and more recognized as a novel technique to investigate high-dimensionality data (51–53). In contrast to highlighting just a minimal subset of predicted output functions, biomedical word clouds create a more holistic representation of the full spectrum of signaling ramifications borne out of the data set(s). In accordance with our transcriptomic analyses (Fig. 2), we found that this unbiased NLP-based data-set interpretation was highly concordant, such that the terms synaptic, postsynaptic, endocytic, axonal, cytoskeleton, and PDZ (Fig. 7*A*) were prominent. To analyze this highly nuanced output impartially, we used the textual analyzer WriteWords (http://writewords.co.uk/).[4] Upon textual frequency analysis we found several words that were disproportionally over-represented (>99% confidence limit of significance using individual word frequency scores (supplemental Table S21)) in this word-

[4] Please note that the JBC is not responsible for the long-term archiving and maintenance of this site or any other third party hosted site.

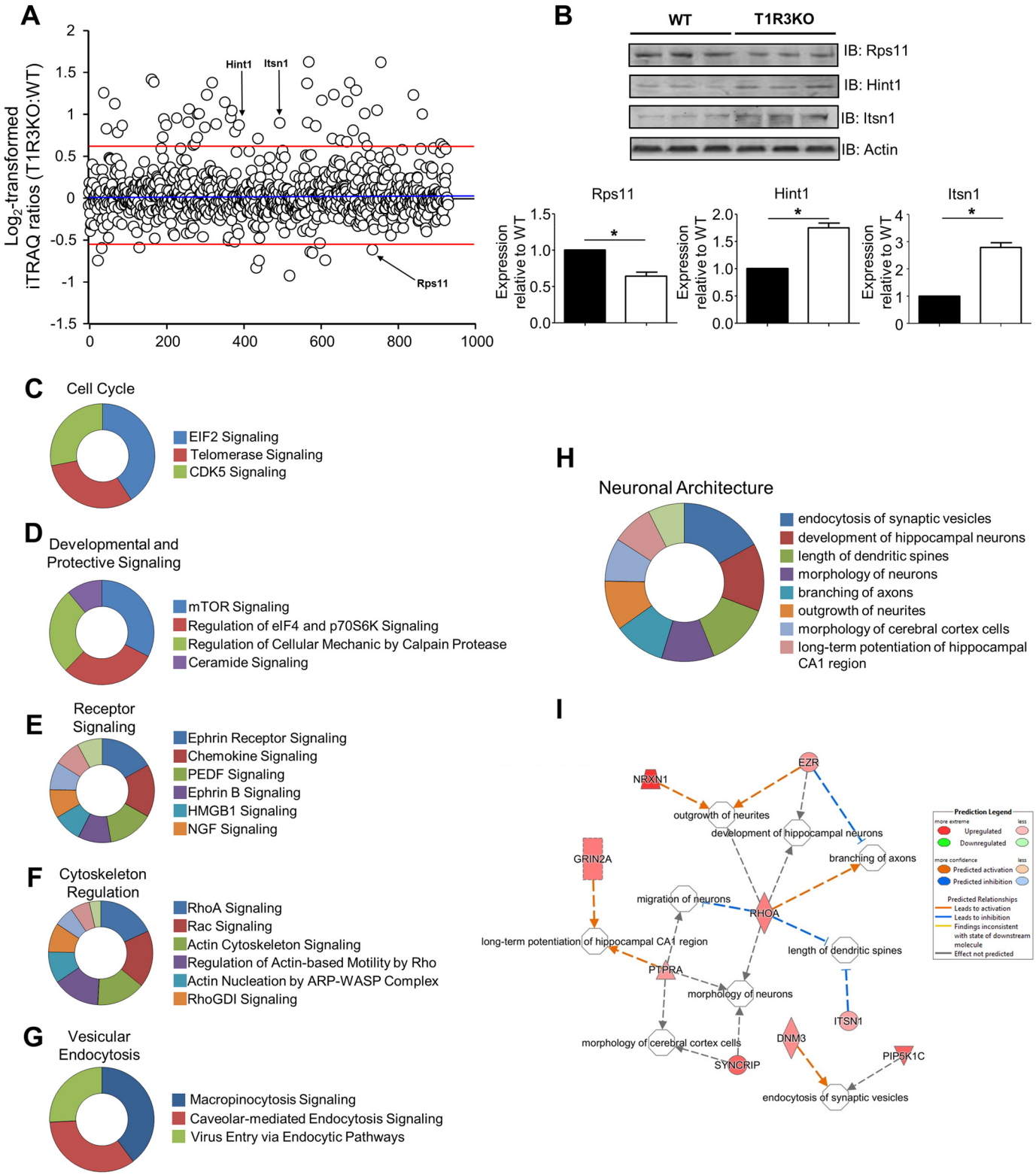

Figure 4. Differential proteomic expression patterns in T1R3KO cortex *versus* WT controls iTRAQ data. *A*, $\log_2$-transformed ratios (T1R3KO:WT) from cortical iTRAQ data are displayed; proteins with significantly differential expression ($p \leq 0.05$) in T1R3KO *versus* WT control are above or below the *red lines*. *B*, Western blot validation of randomly selected proteins differentially expressed in the T1R3KO hippocampus. The iTRAQ-generated expression profiles of Rps11, Hint1, and Itsn1 were all confirmed by Western blotting of T1R3KO and WT mice. Additionally actin-normalized protein expression levels are shown. *Error bars* represent mean ± S.E.; $p \leq 0{,}05$ was considered statistically significant. *C–G*, pie charts depicting the distribution of the canonical signaling pathway groups identified in the T1R3KO data set using IPA according to specific biological functions, *i.e.* cell cycle (*C*), developmental and protective signaling (*D*), receptor signaling (*E*), cytoskeletal regulation (*F*), and vesicular endocytosis (*G*). *H*, pie chart identifying the multiple biofunction/disease pathway annotations of the significant proteomic data. *I*, using IPA-based protein-signaling network generation, the most coherent interactions responsible for the associated T1R3KO biofunctions/diseases (represented in *H*) are highlighted.

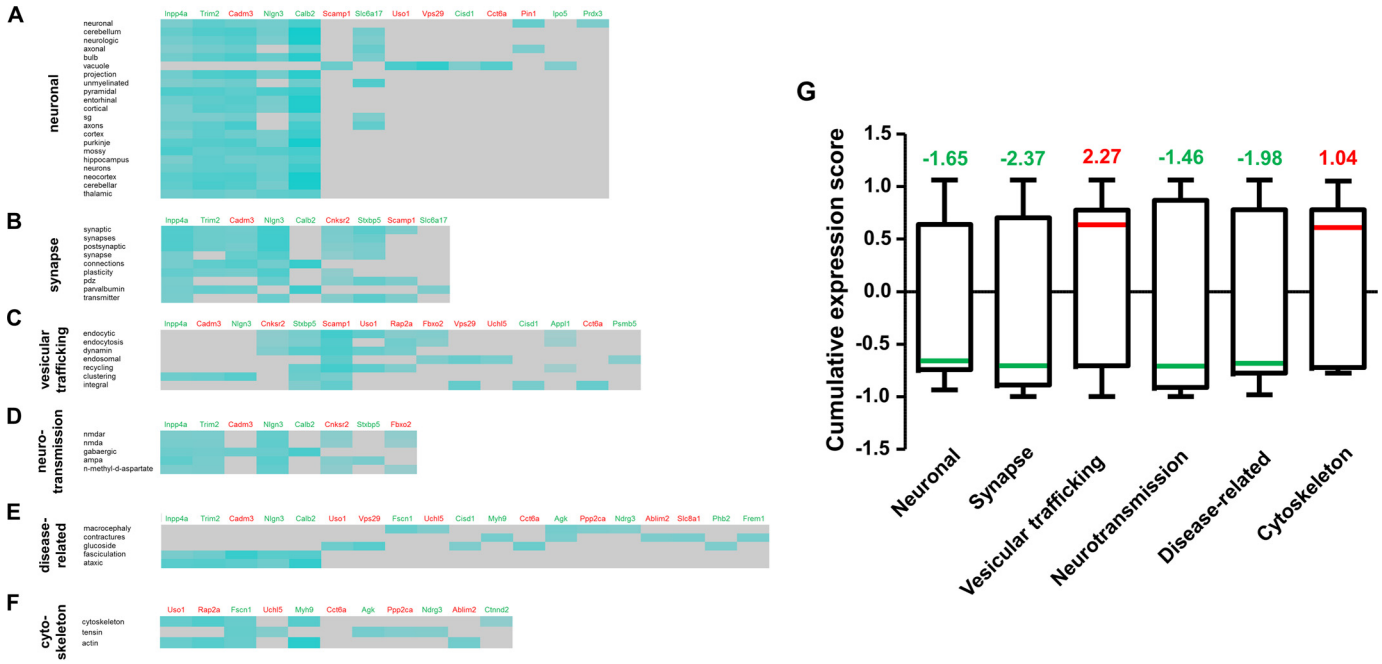

Figure 5. *Textrous!* natural language processing-based interpretation of hippocampal proteomic data. The potential functional relationships between significantly and differentially regulated proteins in T1R3KO hippocampi compared with WT controls were interpreted using the individual processing mode of *Textrous!* Proteins (up- or down-regulated in T1R3KO *versus* WT, indicated in *red* or *green*, respectively) and their correlated biomedical terms are represented as a heat-map matrix, with the strength of association indicated by the intensity of the *teal blocks* and "no correlation" indicated by a *gray block*. Specific functional clusters of protein activity were found using the hippocampal proteomic data set, *i.e.* neuronal (*A*), synapse (*B*), vesicular trafficking (*C*), neurotransmission (*D*), disease-related (*E*), and cytoskeleton (*F*) are depicted. *G*, mean $\log_2$ iTRAQ expression scores (*box* and *whiskers* plot indicates 5–95% confidence limits; the mean score is indicated by either a *red* or *green line* depending on whether the mean possessed a positive or negative sign) for proteins subclassified into the specific functional *Textrous!* groups (*A*–*F*). Above each box the *red* or *green number* indicates the numerical sum of the $\log_2$-transformed iTRAQ expression scores for the proteins identified in that functional *Textrous!* group.

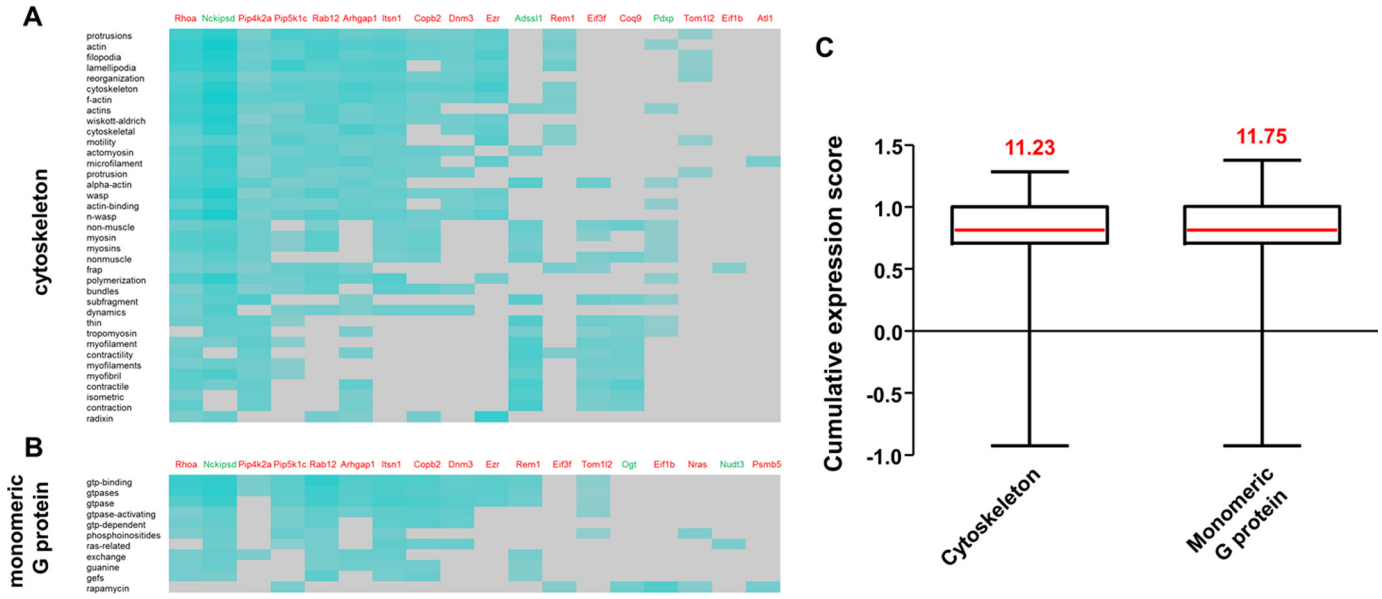

Figure 6. *Textrous!* natural language processing-based interpretation of cortical proteomic data. The potential functional relationships between proteins significantly and differentially regulated in the T1R3KO cortex compared with WT controls were interpreted using the individual processing mode of *Textrous!,* proteins (up- or down-regulated in T1R3KO *versus* WT indicated as *red* or *green*, respectively), and their correlated biomedical terms are represented as a heat-map matrix, with the strength of association indicated by the intensity of the *teal* blocks and "no correlation" indicated by a *gray block*. Specific functional clusters of protein activity were found using the hippocampal proteomic data set, *i.e.* cytoskeleton (*A*) and monomeric G proteins (*B*). *C*, mean $\log_2$ iTRAQ expression scores (*box* and *whiskers* plot indicates 5–95% confidence limits; the mean score is indicated by either a *red* or *green line* depending on whether the mean possessed a positive or negative sign) for proteins subclassified into the specific functional *Textrous!* groups (*A* and *B*). Above each box the *red* or *green number* indicates the numerical sum of the $\log_2$-transformed iTRAQ expression scores for the proteins identified in that functional *Textrous!* group.

cloud output, *i.e.* cortical, neurons, synaptic, cerebellar, and actin (Fig. 7*B*), again supporting our functional interpretations using transcriptomic data from the T1R3KO mice.

In contrast to the hippocampal data analysis, the word cloud interpretation of the cortical proteomic data suggested a less synaptically focused nature of the data, *e.g.* the most prominent

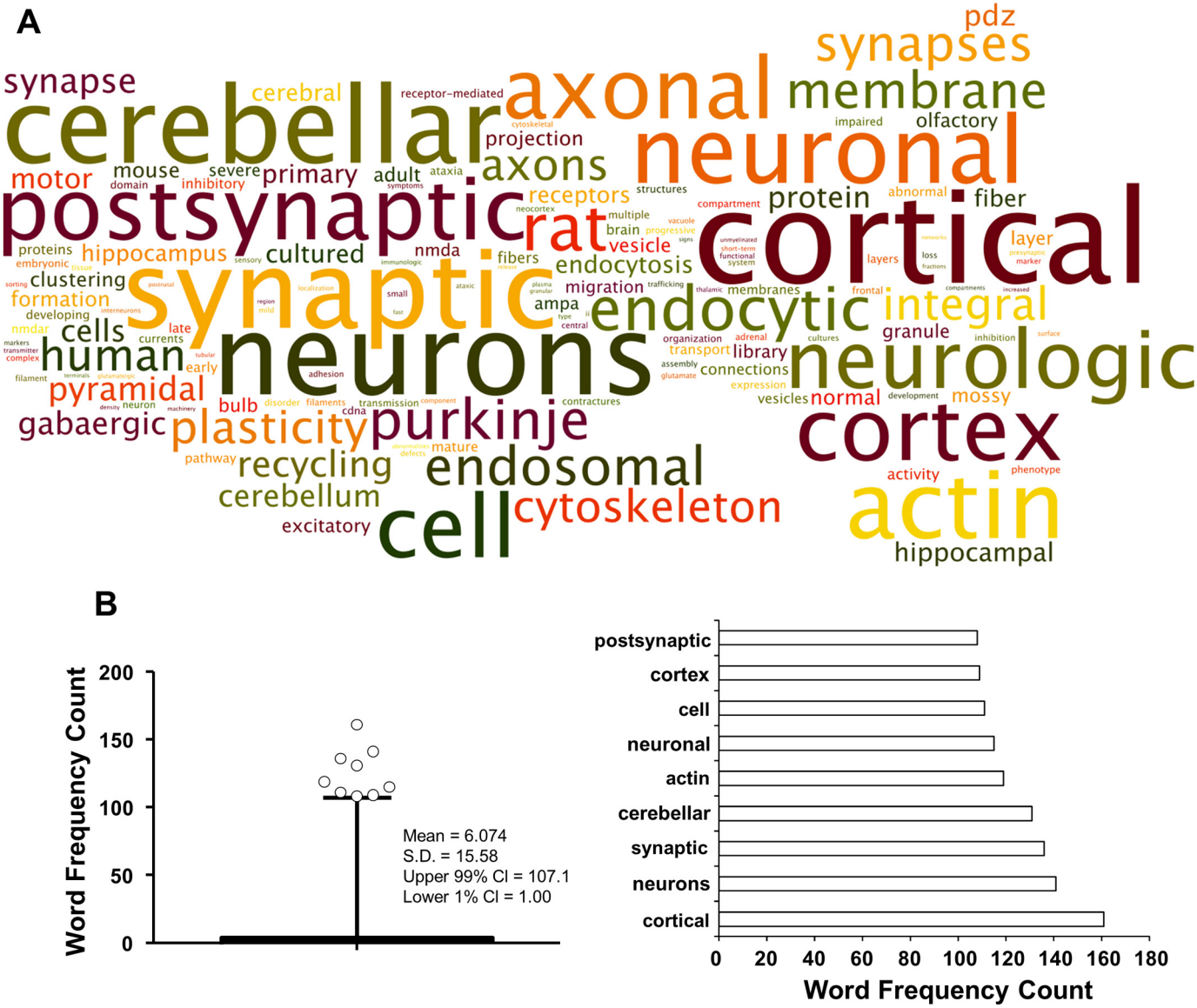

Figure 7. Quantitative high-dimensionality hippocampal proteomic data word cloud. *A*, correlated full noun phrases were extracted from the *Textrous!*-based semantically associated word lists created using the input significantly altered T1R3KO hippocampal proteomes. The font size in the word cloud is directly related to the word frequency present in the extracted noun-phrase lists. *B*, applying word frequency analysis to this semantically associated list, nine specific words significantly ($p \leq 0.01$) overrepresented in the list (*box* and *whiskers* plot indicates 1–99% confidence limits) were identified (*left panel*). The specific word frequency count for these words is represented to indicate their ranking.

words were linked primarily with cytoskeleton-modulating behavior (cytoskeletal, dynamics, actin, motility, and polymerization) (Fig. 8*A*). Using WriteWords-based quantification of the cortical word cloud data, we were able to demonstrate that the significant textual output from these data was linked predominantly to GTPase-associated cytoskeletal regulatory behavior (cytoskeletal, GTPase, exchange, and actin) as opposed to the focused neurosynaptic activity apparent from hippocampal data-set interpretation (Fig. 8*B* and supplemental Table S22).

Altered architectural structure of the T1R3KO hippocampus

As our high-dimensionality data investigation of T1R3KO mice suggested a specific hippocampus-focused neurosynaptic phenotype, we next investigated the effects of genomic T1R3 deletion upon hippocampal neuronal architecture using Golgi staining. Upon inspection of Golgi-stained hippocampal CA1 regions from WT and T1R3KO mice, we noted a considerable increase in hippocampal neuronal density in the T1R3KO mice compared with the WT controls (Fig. 9, *A* and *B*). This distinction in T1R3KO mice appeared to be generated by an increased presence of large neuritic densities (Fig. 9, *C–E* (WT) and *D* and *F* (T1R3KO)). Concomitant with this increased neuritic density we also noted that the T1R3KO dendrites possessed significantly fewer spines across their length (Fig. 9, *G* and *H*). Indicative of the increased neuritic density in the T1R3KO hippocampus, we also found that the average dendrite length in the T1R3KO mice was greater (non-significantly) than in the WT controls (Fig. 9*I*). The evident neuronal somatic "expansion" (Fig. 9, *D* and *F*) is potentially associated with the observed dendritic spine density and alteration of primary dendrite morphology (*i.e.* apparent dendritic collapse). Taken together with

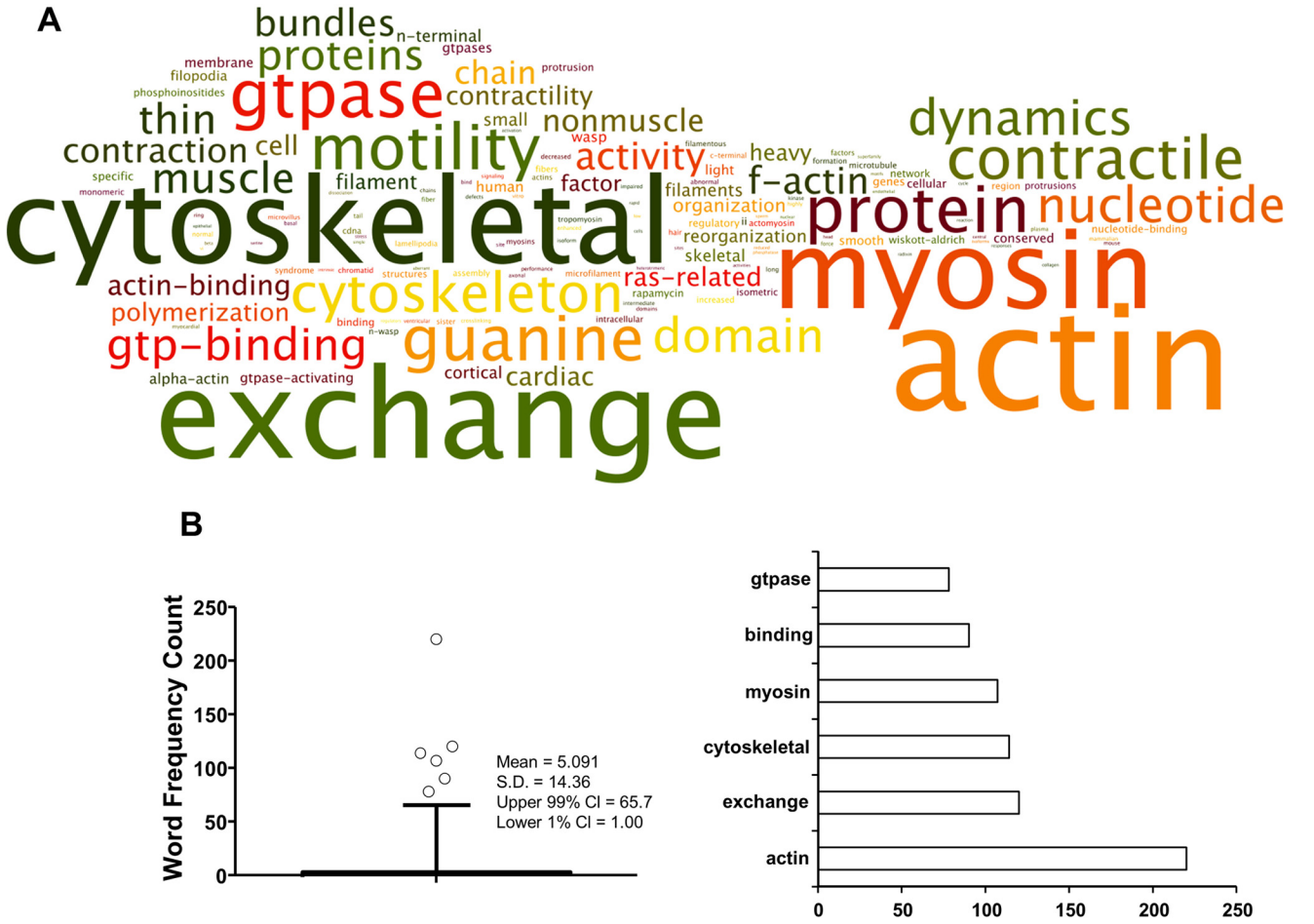

Figure 8. Quantitative high-dimensionality cortical proteomic data word cloud. *A*, correlated full noun phrases were extracted from the *Textrous!*-based semantically associated word lists created using the input significantly altered T1R3KO cortical proteomes. The font size in word cloud is directly related to the word frequency present in the extracted noun-phrase lists. *B*, applying word frequency analysis to this semantically associated list, six specific words significantly ($p \leq 0.01$) overrepresented in the list (*box* and *whiskers* plot indicates 1–99% confidence limits) were identified (*left panel*). The specific word frequency count for these words is represented to indicate their ranking.

the increased neuritic density, reduced spine density, and increased dendrite length, these results suggest a potential neurological dysfunction/synaptic failure in the T1R3KO mice. Reinforcing this conclusion, and perhaps in reactive response to neurosynaptic failure, increases in hippocampal NR1 (NMDA receptor subunit 1 (Fig. 9, *J* and *K*)) and NR2B (NMDA receptor subunit 2B (Fig. 9, *L* and *M*)) expression were observed in T1R3KO mice compared with WT controls. These findings were further supported via Western blotting, which demonstrated significant increases in both the NR1 and NR2B subunits in T1R3KO *versus* WT controls (Fig. 9*N*).

Based on our identification of altered neurosynaptic structure (Golgi staining, Fig. 9, *A–I*) and molecular signaling activity (NR1 and NR2B expression, Fig. 9, *J–N*) in T1R3KO mice, we next investigated whether individual neuronal excitability in the T1R3KO mice was also affected. Primary neurons from both WT and T1R3KO neonatal mice were isolated and cultured for 7 days to allow mature dendrite and axon growth. The fluorescence intensity of cell membrane-permeable Ca^{2+}-binding fluorophore Fluo-8 AM was used as an indicator of intracellular calcium concentration. Using simultaneous microscopic cellular analysis, in response to the addition of 100 μM glutamic acid (Fig. 9*O*), Fluo-8 AM intensity rose quickly after excitatory ligand addition in both WT and T1R3KO neurons with 2–3.5-fold amplitude elevation in fluorophore levels. With respect to intracellular Fluo-8 AM intensity, WT neurons recovered gradually, and the cytoplasmic calcium $[Ca^{2+}]_c$ returned to basal levels after 2–3 min (Fig. 9*P*), whereas the isolated primary T1R3KO neurons remained excited with sustained and elevated $[Ca^{2+}]_c$ for more than 280 s (Fig. 9*Q*). Measuring the mean Fluo-8 AM intensity across the time period of the glutamate stimulation, we found a significant difference in the kinetic profile of stimulated calcium release/management between the T1R3KO and WT neurons (Fig. 9*R*).

Altered neurosynaptic protein expression levels in T1R3KO hippocampus

We next investigated the expression level of proteins specifically involved in neurosynaptic activity in T1R3KO mice. In line with our findings of potentially disrupted neurotransmission in T1R3KO mice (compared with WT controls), we found a significant reduction in phosphorylated cAMP response-element-binding protein (p-CREB), phosphorylated synapsin (p-synapsin or p-Syn1), phosphorylated extracellular-signal-regulated kinase 1/2 (p-Erk1/2), spinophilin (Ppp1r9b), PSD-95 (post-synaptic density protein, 95 kDa), and phosphorylated

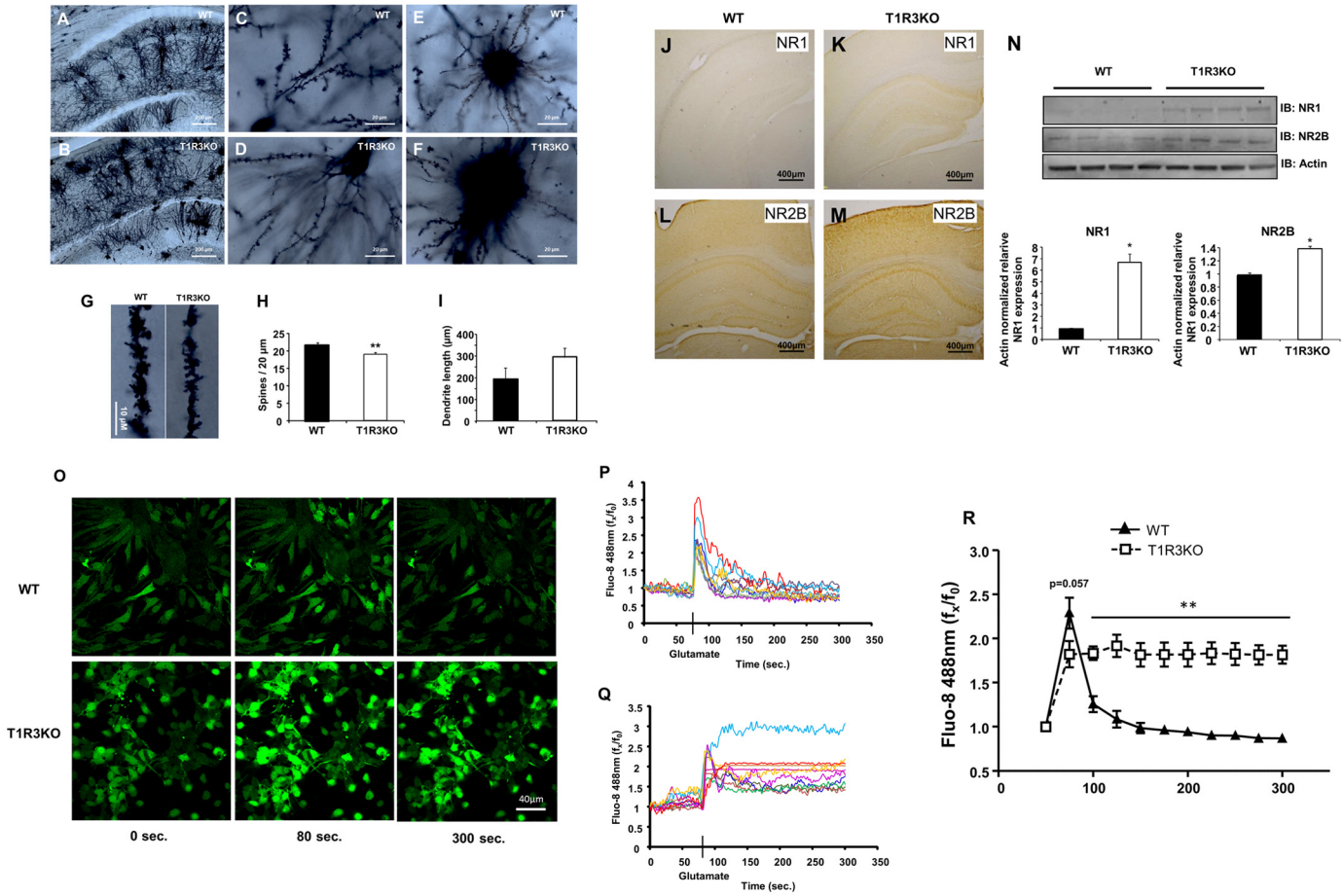

Figure 9. T1R3KO-induced alterations in neuronal architecture and functionality. *A–I*, Golgi staining was performed on 100-μm mouse brain sections. Representative images of the hippocampal CA1 region (*A* and *B*), hippocampal neurons (*C* and *D*), and heavily stained cell bodies (*E* and *F*) are shown. *G*, enhanced images of representative dendritic spine regions in T1R3KO mice *versus* WT controls ($n = 8$ mice/genotype). *H*, mean spine density in T1R3KO mice (*white bars*) compared with controls (*black bars*). *I*, T1R3KO mice demonstrate a non-significant increase in mean dendrite length compared with controls. *J* and *K*, selective immunostaining of NMDA subunit NR1 in hippocampus of WT controls and T1R3KO mice, respectively. *L* and *M*, selective immunostaining of NMDA subunit NR2B in hippocampus of WT controls and T1R3KO mice, respectively. *N*, Western blot verification of selective NR1 and NR2B immunostaining ($n = 4$). T1R3KO mice demonstrate a significant elevation in the hippocampal expression of both NMDA receptor subunits in T1R3KO (*white bars*) mice compared with WT controls (*black bars*). *O*, representative images of both WT and T1R3KO neurons at time zero, 80 s (baseline cytoplasmic calcium level recording) and 300 s after the addition of 100 μM glutamic acid, are shown. *P* and *Q*, 10–12 representative cells were chosen from each experimental group (WT (*P*) or T1R3KO (*Q*)) to indicate the temporal changes of glutamate-induced cytoplasmic calcium concentrations. Each specific cells calcium mobilization pattern in response to glutamate application (indicated by the *black bar* on the time axis) is denoted by a differently colored trace line. *R*, the mean temporal nature of calcium oscillations for WT (*black triangles*) or T1R3KO neurons (*white squares*) was measured and plotted. WT cells demonstrated a transient calcium mobilization response to glutamate, whereas T1R3KO cells were unable to effectively attenuate the ligand-induced calcium mobilization over the 300-s time period. *Error bars* represent mean ± S.E.; $p \leq 0.05$ was considered statistically significant.

TrkB (p-TrkB) (Fig. 10). The reductions in the levels of these factors all pointed to an effective neurotransmission deficit in the T1R3KO mice compared with WT controls. We also further investigated the same protein expression profile in cortical tissues in both T1R3KO and WT mice (Fig. 10). Reinforcing the specific hippocampal nature of these deficits in T1R3KO mice, although similar cortical expression trends were apparent (*e.g.* p-synapsin 1 and spinophilin), no significant alterations in this same panel were found in T1R3KO cortex samples.

Deficits of learning and memory function in T1R3KO mice

Our multidimensional interpretation of both transcriptomic and proteomic data from the T1R3KO mice generated a focused assessment of potential physical and functional neurosynaptic dysfunction in these mice. We next investigated whether these phenotypic molecular "signatures" would also be predictive of actual disrupted cognitive/behavioral activity in these mice. We employed both novel object preference (NOP) and Morris water maze (MWM) tests to assess learning and memory functions in T1R3KO mice.

Using the NOP test we found that, unlike with WT mice, T1R3KO mice did not demonstrate a significant preference for novel objects (Fig. 11*A*), resulting in a significantly lower discrimination index in the T1R3KO mice for novel objects compared with WT control mice (Fig. 11*B*). Using the MWM test to assess spatial learning and memory performance we found that, compared with WT control mice, T1R3KO mice demonstrated a significantly longer escape latency time at days 3–4 of MWM training (Fig. 11*C*). Additionally, we found that T1R3KO mice demonstrated a significantly increased swim speed (Fig. 11*D*) and swimming path length (Fig. 11*E*) in the MWM test on days 3–4 compared with WT controls. With the transition from a hidden platform to probe trials in the MWM test, we found that T1R3KO mice spent signifi-

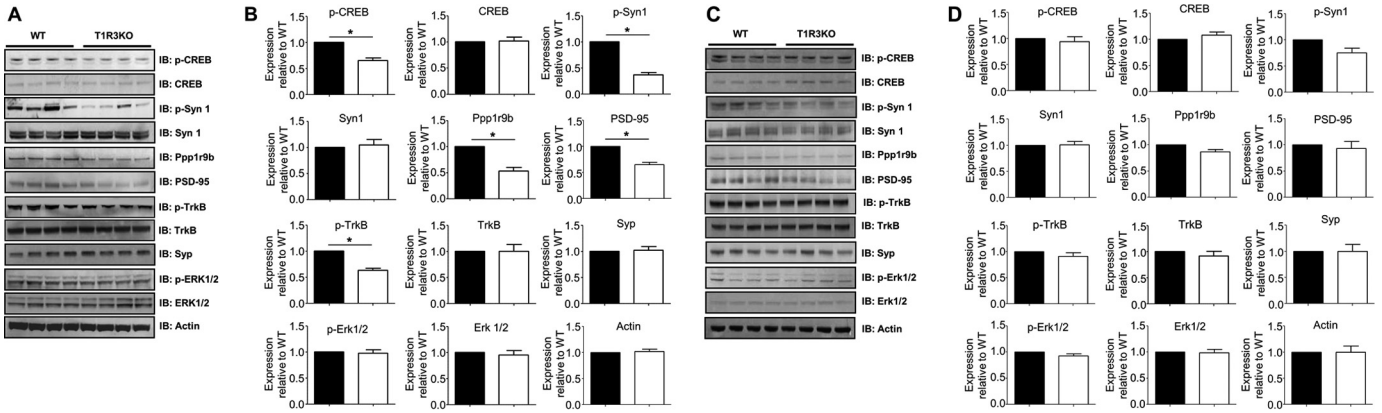

Figure 10. Genomic deletion of T1R3 results in significant alterations in multiple neurosynaptic proteins. *A*, selective Western blot analysis of standard marker proteins indicative of neurosynaptic functionality was performed in T1R3KO and WT mouse hippocampal extracts ($n = 4$ mice/genotype). *B*, compared with WT tissue expression (*black bars*), T1R3KO hippocampal levels (*white bars*) of phosphorylated CREB (*p-CREB*), phosphorylated synapsin 1 (*p-Syn1*), spinophilin (*Ppp1r9b*), PSD-95, and p-TrkB were significantly reduced. No significant differences between WT and T1R3KO tissues in the expression levels of non-phosphorylated CREB, Syn1, TrkB, or Erk1/2 were noted. Levels of synaptophysin (*Syp*) and non-phosphorylated Erk1/2 were also unchanged between WT and T1R3KO tissues. In contrast to the effects of T1R3 deletion in the hippocampus, genomic deletion of T1R3 results in subtle non-significant alterations in multiple neurosynaptic proteins. *C*, selective Western blot analysis of standard marker proteins indicative of neurosynaptic functionality was performed in T1R3KO and WT mouse cortical extracts. *D*, compared with WT tissue expression (*black bars*), T1R3KO hippocampal levels (*white bars*) of phosphorylated synapsin 1 showed a strong (non-significant) trend toward reduced expression. For the other constituents of the neurosynaptic protein panel investigated previously (Fig. 9), no strong differences in expression were noted between WT or T1R3KO tissues. *Error bars* represent mean ± S.E.; $p \leq 0.05$ was considered statistically significant.

cantly less time in the MWM quadrant that housed the platform previously (Fig. 11*F*).

Altered social and behavioral activity in T1R3KO mice

With the evident association with appetitive taste perception and behavioral modalities (36), we next assessed whether genomic T1R3 deletion affected social and behavioral activity. Using the classical three-chambered sociability test we found that T1R3KO mice, unlike the WT controls, failed to demonstrate a significant preference for interaction with an animate target mouse compared with an inanimate target (Fig. 11*G*). This resulted in the generation of a significantly lower discrimination index for the T1R3KO mice compared with WT controls for social interaction (Fig. 11*H*).

Further behavioral distinctions were observed between T1R3KO and WT mice using the open field test. T1R3KO mice demonstrated significantly lower ambulatory distance (Fig. 11*I*) and significantly greater physical inactivity (Fig. 11*J*), as well as a significantly greater propensity to spend time in the periphery of the field and less time in the field center (Fig. 11*K*). Related to this final finding, we also observed a significantly reduced propensity for T1R3KO mice, compared with WT controls, to remain in the light zone of the open field, coupled to a concomitant increase in their time spent in the open field dark zone (Fig. 11*L*). Assessing stress/anxiety using the elevated plus maze demonstrated only a subtle (non-significant) propensity for T1R3KO mice to spend more time in the closed arms rather than the open arms, compared with WT controls (Fig. 11*M*). Although they demonstrated multiple neuropsychological and behavioral deficits, the T1R3KO mice, compared with WT controls, displayed no motor coordination deficits using the Rota-Rod test (Fig. 11*N*).

Discussion

It is becoming clear that in addition to our deeper appreciation of the neuroendocrine complexity of taste perception, the sweet-taste receptor system is expressed in many organs other than the tongue (3, 24, 36, 54–57). Here we have demonstrated that loss of the T1R3 subunit causes learning and memory impairments, CNS synaptic failure, attenuated neurotrophic activity, and proteomic molecular signatures and behavioral activities reminiscent of neurodegenerative phenotypes.

Despite research indicating a role of somatic metabolic hormones in taste perception, we found no significant metabolic disruption in T1R3KO mice (Fig. 1, *B–E*). These observations, however, do not necessarily preclude the capacity for these animals to generate a metabolic phenotype later in life. Our transcriptomic (Fig. 2), proteomic (Figs. 3–8), neurosynaptic (Figs. 9 and 10), cognitive, and psychosocial and behavioral investigations (Fig. 11) of T1R3KO mice however suggested a strong pro-neurodegenerative impact of T1R3 genomic deletion. CNS transcriptome profiling can generate an effective appreciation of complex functions such as neurodegeneration (45) and pathological aging (48). T1R3KO transcriptomic profiling demonstrated a greater coherency between cortical/hippocampal tissues compared with hypothalamic tissues (Fig. 2); this may underpin the relatively greater importance of CNS dysfunction (Figs. 2–4) *versus* somatic metabolic functions (Fig. 1) to the T1R3KO mouse phenotype. With specific reference to the strongest scoring hippocampal bio-function prediction, *i.e.* "proliferation of neuronal cells," the factors populating this group consisted of multiple transcripts linked to Alzheimer's disease (AD) (K-Ras (58), Wnt7b (59), Rasgrf1 (60), and Tardbp (61, 62)), calcium-dependent hippocampal neuronal excitability (K-Ras (63)), neurogenesis (Socs2 (64), Rasgrf1 (65), Bmpr1a (66), Id4 (67), and Dcx (68)), synaptic and dendritic development (Brsk2 (69), Wnt7b (70, 71), Rasgrf1 (60), Vgf (72), Cnp (73), Dcx (74), Rnf6 (75), Sema3a (76), and Tsc2 (77)), neuroprotective activity (Cbr1 (78)), anxiety-related behavior (Cxcl12 (79) and Tsc2 (80)), and learning/memory functions (Xpa (81), RasGrf1 (82), and Ccnd1 (83)). Proteomic analyses of

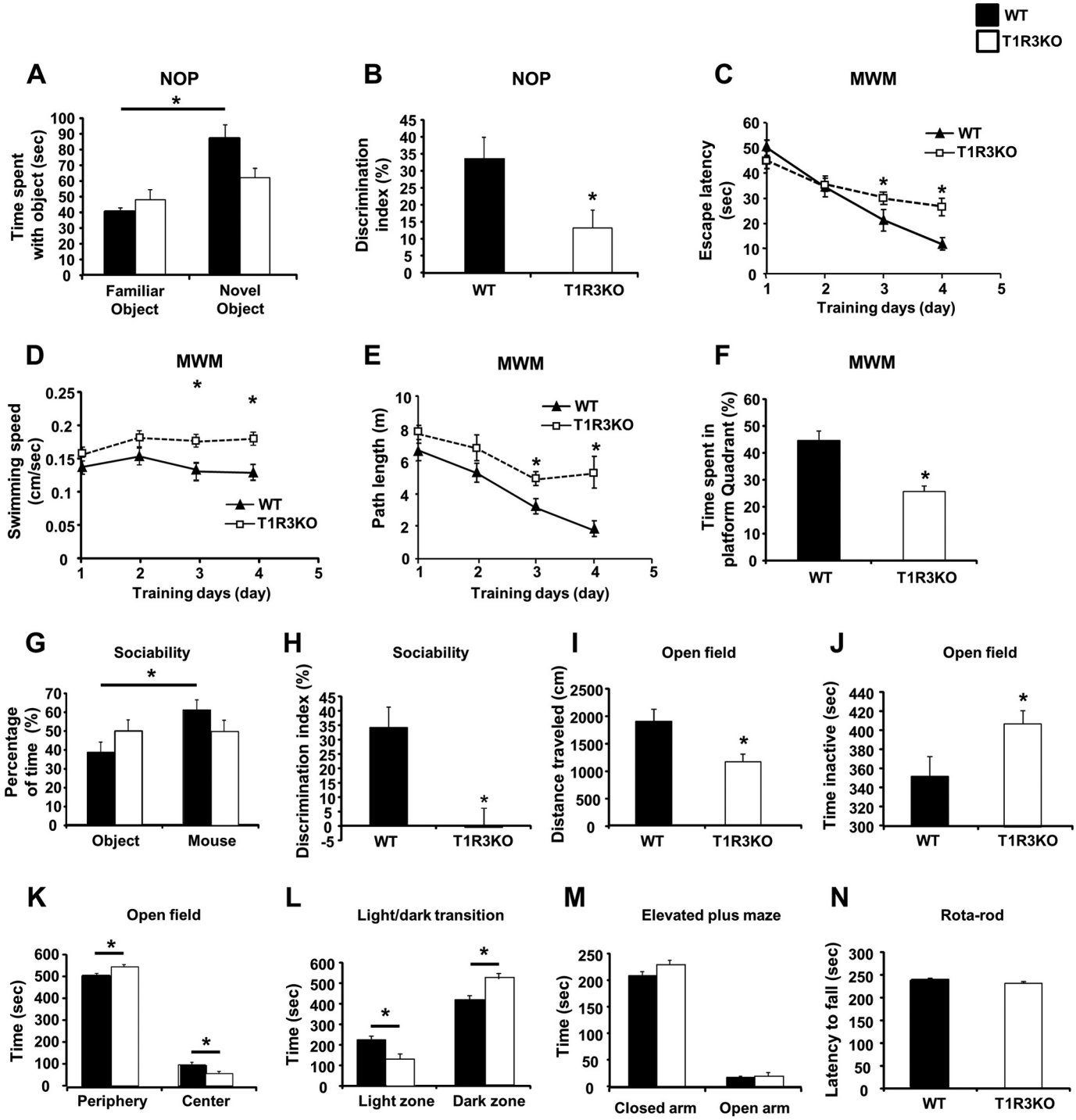

Figure 11. Impaired cognitive, social, and exploratory behavior in T1R3KO mice compared with WT controls ($n = 8$ mice/genotype). *A* and *B*, recognition memory was assessed using NOP (WT, *black bars*; T1R3KO, *white bars*). *A*, time spent investigating familiar or novel objects. *B*, discrimination index in percentage of T1R3KO mice compared with WT controls. *C–F*, spatial learning was assessed using MWM tests to measure escape latency (*C*), swimming speed (*D*), path length (*E*), and percentage of time spent in (target) platform (*F*). T1R3KO mice required more time to find the escape platform (*C*), even though the swimming speed (*D*) and the path length (*C*) significantly increased during the last 2 days of training (*E*). In the probe task, WT mice spent 44.67% of the total time in the quadrant where the platform was placed compared with 25.64% of total time for T1R3KO mice (*F*). *G*, sociability was evaluated using the three-chamber social behavior apparatus. Compared with WT controls, T1R3KO mice had no preference in staying with another mouse and showed a lower discrimination index (*H*). Anxiety levels were analyzed using an open-field test (*I–K*), light/dark transition test (*L*), and elevated plus maze (*M*). The open-field test was analyzed with respect to distance traveled (*I*), time inactive (*J*), and time spent in periphery/center of the field (*K*). T1R3KO mice showed lower activity in the open field (*I–K*) and spent more time at the peripheral area of the chamber (*K*). *L*, T1R3KO mice stayed significantly longer in the dark zone compared with the controls. *M*, the elevated plus maze analysis showed no difference in time spent on the open/closed arm, indicating an absence of anxiety behavior in T1R3KO mice. *N*, Rota-Rod analysis showed no significant difference between T1R3KO mice and controls. In each experiment the T1R3KO mice (*white*) were compared with the WT controls (*black*). *Error bars* represent mean ± S.E.; $p \leq 0.05$ was considered statistically significant.

hippocampal and cortical tissues further demonstrated significant alterations in multiple proteins associated with neurodegenerative conditions (Nrxn1 (84) and Pin1 (85), Prdx3 (86)), psychosocial disorders (Agk (47), Arhgap18 (87), and Itsn1 (88)), and pathological aging (Nlgn3 (89), Ipo5 (90), and Ogt (91)). Through classical pathway-based informatics, a profound alteration in neuronal architecture (Figs. 3–8) linked to dysfunctions in neuritogenesis, dendritic growth, and hippocampal neuronal morphology was evident in the T1R3KO mice, together with the concerted activity of multiple significantly regulated proteins. *Textrous!*-based natural language processing of our proteomic data demonstrated that reductions in neuronal, synaptic, and neurotransmissive functionalities were likely (Fig. 5*G*). Using Golgi staining we confirmed these informatic predictions, *i.e.* we found cortico-hippocampal neurodendritic clumping, poor spatial synaptic connectivity, and a significantly reduced dendritic spine density in T1R3KO mice (Fig. 9). Neurosynaptic architecture deterioration is strongly linked with cognitive dysfunction and memory loss in neurodegenerative diseases such as AD and FTD (92–94). Excitatory postsynaptic terminals are associated with dendritic spines (95–97). Calcium influx into these spine heads, through NMDA-type glutamate receptors, is well known to induce long-term potentiation, which underpins hippocampal learning and memory formation (98–100). Furthermore, dendritic spines undergo activity-dependent remodeling to support synaptic plasticity and learning/memory function (101–103). Because alterations in synaptic marker expression and phosphorylation are indicative of abnormalities in synaptic vesicle dynamics, long-term potentiation, and impaired memory function (104, 105), the synaptic markers that were found downregulated in the T1R3KO mice (*i.e.* synapsin 1, synaptophysin, spinophilin, and PSD-95) can be interpreted as critical indicators of cognition (106–110). PSD-95 knock-out mice demonstrate spatial memory impairment due to the excessive excitation of synapses (111). Reduced PSD-95 expression levels are also correlated with disease severity for multiple neurodegenerative conditions such as AD (112), mild cognitive impairment (113), FTD (114), Huntington's disease (115), and pathological aging (116). Spine loss and subsequent spinophilin reductions are also evident in multiple transgenic murine models of neurodegeneration, *e.g.* AD (117–119) and advanced aging (120). Reductions in synaptic spinophilin are also strongly correlated with neurodegenerative disease pathology progression rates (121) as well as with the severity of learning and memory deficits (122).

In addition to dendritic spine disruption, our observed upregulation of post-synaptic NMDA glutamate receptors (NR1/NR2B) is a potential indication of denervation supersensitization, *i.e.* reflexive potentiation of receptor expression (123), occurring due to a reduction of a coherently regulated stimulating input. Linked to this we also found altered responsivity to glutamate in T1R3KO mice, indicative of a disrupted calcium sequestration and storage functionality (Fig. 9), a process strongly linked with neurodegeneration (124, 125) and pathological aging (126).

Synaptic plasticity requires both neurotrophic ligand support and the regulation of rapid protein translation. Hence an interplay exists between neurotrophins, such as brain-derived neurotrophic factor (127) and nerve growth factor and transcriptional/translational controllers such as CREB (128, 129)), Erk1/2 (130, 131), and upstream transcription factor 1 (Usf1 (132, 133)). T1R3KO mice demonstrated significant reductions in hippocampal CREB phosphorylation as well as TrkB phosphotyrosine content (Fig. 10). A similar but non-significant trend for the reduction in these factors was also observed in T1R3KO cortical tissues (Fig. 10). CREB forms a convergence point of pathways and mechanisms activated during the processes of synaptic strengthening, plasticity, and memory formation, as CREB phosphorylation leads to the transcription of memory-associated genes (134). The reduced levels of CREB/TrkB phosphorylation in the T1R3KO mice suggest an extant deficit in memory formation and/or brain-derived neurotrophic factor signaling in these animals.

When we investigated the potential behavioral effects of the multiple neurodegenerative indices identified in our study, we found that T1R3KO mice demonstrated impaired acquisition of novel objects as well as an impaired acquisition and learning of cognitive tasks (Fig. 11). T1R3KO mice also presented blunted sociability, reduced exploratory behavior, and moderately elevated anxiety responses (Fig. 11). Impaired sociability and restricted interests are hallmarks of autism spectrum disorder (ASD) and are strongly linked to disrupted neurosynaptic architecture. T1R3KO mice demonstrated behavioral (Fig. 11) and molecular transcriptomic (supplemental Tables S1–S3)/proteomic (supplemental Tables S13 and S14), signatures associated with ASD-like phenotypes. T1R3KO mice demonstrated alterations in multiple factors linked to ASD etiology in the murine BTBR T+tf/J inbred mouse strain model, *e.g.* reductions in cortistatin along with elevations in Cadm3 and Wfs1 (47). Neuroligin 3 (Nlgn3), a post-synaptic cell-surface protein associated with ASD (135), was significantly reduced in the T1R3KO hippocampus. Neuroligins are trans-synaptic ligands for pre-synaptic neurexins and may be involved in the formation and remodeling of CNS synapses. Interestingly, we found a significant elevation of cortical Nrxn1 in the T1R3KO mice. Impaired regulation of neuroligin-neurexin connectivity at glutamatergic synapses appears to be crucial in ASD-related pathophysiology (136). In autistic patients, an increased neuron excitation/inhibition ratio has been found associated with the pathology of neural dysfunction (137), again reminiscent of our observed altered T1R3KO primary neuron responsivity to glutamate (Fig. 9).

Our NOP/MWM data suggested that neurosynaptic failure, a common feature of dementias such as AD (138) and FTD (139), likely contributes to the cognitive deficits observed in T1R3KO mice. Our T1R3KO hippocampal proteomic signatures identified a significant reduction in the vesicular trafficking protein γ-taxilin (Txlng), which has recently been implicated in stress-induced AD-related tauopathy formation (140). Hotokezaka *et al.* (140) have demonstrated that Txlng is stress-responsive and vital for maintaining the integrity of the unfolded protein response system. Genetic ablation of Txlng expression in neuronal cells has thus been shown to induce AD-related Tau hyperphosphorylation. Tau pathologies in AD are also linked to amyloid deposition via Pin1 (peptidyl-prolyl

cis-trans isomerase NIMA-interacting) (141–143). Pin1 activity prevents neurons from exiting their post-mitotic state and pathologically re-entering the cell cycle. We observed a significant elevation of T1R3KO hippocampal Pin1, which may indicate a reflexive response to prevent excessive amyloid and tau pathologies. Pin1 overexpression is involved in the degradation of wild-type Tau as seen in AD (144) and FTD with parkinsonism linked to chromosome 17 (FTDP-17) (145). Unlike AD, FTD patients often present first with significant social/syntactic abnormalities prior to the later onset of cognitive decline/memory loss. In this respect the combination in the T1R3KO model of (i) altered social interactions, (ii) cognitive decline, and (iii) neuronal dysfunction presents a potentially intriguing murine insight into this condition. FTD is also strongly associated with NMDA receptor dysfunction (146), seen in the T1R3KO mice; NMDA receptor antagonists are also considered potential therapeutic strategies for FTD (146). We also noted from our proteomic T1R3KO signatures a significant reduction in the putative L-DOPA (L-3,4-dihydroxyphenylalanine) receptor (ocular albinism type I (OA1)/Gpr143). Dysfunctions in the dopamine and L-DOPA signaling systems have been strongly associated with FTD etiology (139, 147–149). OA1 is a discrete L-DOPA receptor, and given that FTD is often presented with linguistic abnormalities it is interesting to note that L-DOPA has been demonstrated to engender a highly specific semantic nootropic effect (150, 151). We also noted a significant reduction in hippocampal T1R3KO expression of Slc6a17 (sodium-dependent neutral amino acid transporter Slc6a17), in which homozygous mutations are linked with FTD-like neuropathologies including, diminished cognitive ability, linguistic degradation, and psychosocial deficits (152). Effective loss of this protein has also been correlated with disruptions in dendritic spine formation and perturbations of glutamatergic signaling patterns, both features evident in the T1R3KO mice (153).

Using ourWordCloud-based appreciation of the differential effects of T1R3 loss between hippocampal and cortical tissues, it was evident that a strong cerebellar component of the resultant pathophysiology was prominent (Fig. 7*A*). Recent research has suggested that in addition to its classical role in fine-motor control, the cerebellum may also possess a higher cognitive functional role (154–157). The cerebellum has also been implicated as a functional locus in cognitive/psychosocial disorders such as ASD (158), a role controlled by physical communication tracts between the hippocampal/amygdalic regions and the cerebellum itself (159). Further research into this potential hippocampal-cerebellar axis may prove fruitful for identifying novel multifunctional neurotherapeutics.

In addition to the demonstration of dementia-like cognitive and social deficits, T1R3KO mice also demonstrated some degree of reluctance to explore an open field, potentially indicative of a spatial anxiety. As with the altered Nlgn3-Nrxn1 stoichiometry described previously, we also observed an intriguing differential expression pattern of Hint1 in T1R3KO mouse tissues, *i.e.* significant hippocampal reductions combined with significant cortical elevation. A similar cortico-hippocampal expression divergence for Hint1 is associated with perturbed social behavior in mice (160), and Hint1 knock-out mice demonstrate heightened levels of anxiety-related behavior (161).

Our data reported here demonstrate the complex multidimensional impact that loss of the T1R3 exerts upon neuronal functionality. Further research into this paradigm should now be focused perhaps on a more reductionist approach, to piece together the physical molecular connectivity between our phenomenological results and the actual sweet-taste heterodimer receptorsome structures themselves (162).

Considering our data, which ranges from alterations in molecular signatures in the CNS, to neuronal architecture, *in vitro* cellular signaling activity, and behavioral modifications, it is evident that the sweet-taste receptor system likely plays a multidimensional role in cognitive, psychosocial, and neuroprotective activities in the brain. This concept then necessitates further investigation into the role of this receptor system in complex processes such as neurometabolic aging and dementia, and its future therapeutic exploitation may demonstrate important efficacy profiles for multiple disorders linking the glucose-sensory/metabolic system and cognitive/psychosocial health.

Experimental procedures

Animal care and use

All animal procedures were approved by the Animal Care and Use Committee (ACUC) of the NIA, National Institutes of Health. T1R3KO mice (8), kindly provided by Dr. Charles Zuker (Columbia University), were cross-bred with WT C57BL/6J mice (The Jackson Laboratory) for at least four generations. All animals were kept in a 12-h light/dark cycle and received food (standard Harlan-Teklad chow, LM-485) and water *ad libitum*. A total of 10–20 mice (4–5 months of age) in each group were employed for behavioral, histological, and protein expression analyses. These 4–5-month-old animals were used in experiments and euthanized right after the experiments. For *post mortem* tissue extraction, animals were humanely euthanized with isoflurane, and specific organs/tissues were then carefully dissected, snap-frozen, and stored at −80 °C until further analysis.

Murine behavior assessment

The assessment of general activity levels, exploratory behavior, and locomotor activity in T1R3KO mice compared with control WT mice was performed using an open-field test as described previously (163). Open-field activity-monitoring software (ANY-Maze, Stoelting Co., Wood Dale, IL) automatically recorded multiple parameters over the duration of the 10-min test.

Anxiety-related behavior was assessed using a light-dark transition assessment as well as performance in an elevated plus maze. The light-dark transition test was performed as described previously (164). The square chamber used in the open-field test was also used to complete this test, with the additional insertion of a dark chamber occupying up to 50% of the apparatus area. Time spent in either the light or dark compartment was automatically recorded by the ANY-Maze monitoring software (Stoelting). The elevated plus maze (San Diego Instruments, San Diego) consisted of two open arms and two closed arms that extended from a common central platform;

the experiment was performed as described previously (163). Each mouse was placed in the center square facing an open arm and allowed to freely explore the apparatus for 10 min. ANY-Maze behavioral tracking software was used to record time spent in either the closed or open arms of the apparatus, and the relative time spent in the closed or open arms was calculated by dividing the time spent in either arm by the total exploration time (600 s for all animals).

Social behavior was assessed using a three-chambered sociability apparatus (Stoelting) with a protocol based upon previously established methods (165). Another mouse of the same strain, age, and gender and an inanimate object housed in identical wire-mesh containers were placed in opposing chambers of the apparatus. Experimental animals were then returned to the center chamber of the apparatus where they were free to interact with either the mouse or object. Interactions were recorded for 10 min and analyzed with ANY-Maze monitoring software. A discrimination index taking into account the relative exploration times between the target mouse and the inanimate object, was calculated.

Differences in learning and memory between T1R3KO and WT mice were investigated using both the NOP and MWM tests as described previously (163). For the NOP test, both the habituation session and the testing session were videotaped and the animal's behavior was tracked automatically by ANY-Maze monitoring software. The discrimination index between the two objects was calculated. The MWM was used as described previously (163) to further assess cognitive function. After 4 days of training, animals were given a probe trial on day 5 in which the platform was removed from the pool and the amount of time spent in each quadrant was recorded within 1 min. The probe trial indicates whether the animal can remember in which quadrant the escape platform was located previously. The escape latency, swimming path length, and swimming speed of each animal during each trial were also recorded and analyzed.

Motor coordination was evaluated using an accelerating Rota-Rod treadmill (Med Associates Inc., St. Albans, VT) as described previously (164). On the test day, the mice were placed on the Rota-Rod, which gradually accelerated from 4 to 40 rpm over the 5-min test time. The test was performed twice/day, and the latency to fall was measured and averaged.

Gustatory activity assessment

Taste-testing experiments took place during daylight hours in a manner similar to that described previously (1, 164). T1R3KO and WT mice ($n = 8$/testing group) were habituated to the laboratory environment for 35 min each experimental day before the initiation of taste testing. Test stimuli consisted of various concentrations of sucrose (1, 3, 10, 30, and 100 mM, Fisher Scientific, Atlanta, GA) or sucralose (0.001, 0.01, 0.1, 1, and 5 mM, Toronto Research Chemicals, Toronto, Canada). Brief-access taste-testing took place in a Davis Rig gustometer (Davis MS-160, DiLog Instruments, Tallahassee, FL), as described previously (166–169). Brief-access procedures minimize post-ingestive effects that may confound other assays such as intake tests (168). Before taste-testing was initiated, mice were trained to lick a stationary tube of water in the gustometer after being placed on a 24-h restricted water-access schedule. For appetitive stimuli (*i.e.* sucrose and sucralose) animals received 3 days of testing with the five stimulus concentrations and purified water. A water rinse presentation (1 s) was interposed between the test trials for normally avoided stimuli to help control for potential carryover effects of the agents.

Western blot analyses

Brain tissues were lysed in a modified radioimmune precipitation assay buffer (150 mM NaCl, 50 mM Tris, 0.5% sodium deoxycholate, 1% Nonidet P-40, and 1% SDS). Subcellular fractionation (into the cytosolic, plasma membrane, large organelle, and cytoskeleton compartments) of brain tissues was performed using the Qproteome® cell compartment kit according to the manufacturer's instructions (Qiagen, Valencia, CA). All protein extracts were quantified using BCA reagents (Thermo Fisher Scientific) before resolution with SDS-PAGE and electrotransfer to PVDF membranes (PerkinElmer Life Sciences). Membranes were blocked with 5% nonfat milk and incubated overnight at 4 °C using primary antibodies. After a 1-h incubation with the appropriate secondary antibody, membranes were developed and scanned by a Typhoon 9410 variable-mode phosphorimaging machine. Blots were probed with the following antibodies: rabbit anti-spinophilin, mouse anti-NR1, and rabbit anti-NR2B from Millipore (Billerica, MA); rabbit anti-phospho-CREB, rabbit anti-CREB, rabbit anti-phospho-ERK1/2, rabbit anti-ERK1/2, rabbit anti-phospho-synapsin1, rabbit anti-synapsin1, rabbit anti-synaptophysin, and rabbit anti-PSD95 from Cell Signaling Technology, Inc. (Danvers, MA); rabbit anti-CPLX1 and rabbit anti-HINT1 from Abcam (Cambridge, MA); rabbit anti-SLC8A1 from Epitomics (Burlingame, CA); and mouse anti-β-actin from Sigma-Aldrich. The experiments were repeated at least three times. Results were normalized to actin expression.

Immunohistochemistry

Animals were anesthetized with carbon dioxide and transcardially perfused with 4% paraformaldehyde. Brains were postfixed overnight in 4% paraformaldehyde and then cryoprotected in 30% sucrose and stored at 4 °C until use. Whole brains were sectioned (40 μm) using a Cryotome™ cryostat (Thermo Fisher Scientific). The sections were then processed for immunohistochemical localization of NR1 and NR2B (mouse anti-NR1 and rabbit anti-NR2B) using a Vectastain Elite ABC kit (Vector Laboratories, Burlingame, CA) and developed using a Dako liquid diaminobenzidine chromogen system (DakoCytomation California, Carpinteria, CA). Sections were imaged with an Olympus Fluoview IX70 microscope (Olympus America, Center Valley, PA).

Brain Golgi staining

Brains were processed for Golgi-Cox staining using an FD Rapid GolgiStain™ kit according to the manufacturer's instructions (FD NeuroTechnologies, Columbia, MD). 100-μm coronal sections were sliced on a cryostat and mounted onto gelatin-coated glass slides. After development in NH_4OH for 10 min, sections were dehydrated through a series of graded ethanol washes and cleared in 100% Histo-Clear (National Diagnostics, Atlanta, GA) three times. Slides were then coverslipped

with Permount™ mounting medium (Fisher Scientific) and dried in the dark for at least 1 week. Neurons within the hippocampal CA1 region, fully impregnated with the Golgi-Cox solution, were selected for further analysis using Neurolucida Version 8 software (MBF Bioscience, Williston, VT). These chosen neurons were not obscured by neighboring neurons and had no obviously truncated dendrites. For each animal ($n = 8$), six representative neurons were traced throughout the sections using a Leica DMRB microscope ×100 (NA 1.30) lens. Dendritic spine density and dendrite length were analyzed using Neurolucida Explorer software (MBF Bioscience).

Primary neuron culture

Cortical neurons were prepared from WT and T1R3KO embryonic mice on day 16 as described previously (163). In brief, cells were dissociated by incubation with TrypLE™ Express (Life Technologies, Inc.) at 37 °C for 25 min. Tissues were washed twice with ice-cold Hanks' balanced salt solution (Sigma-Aldrich) after the addition of minimum essential medium containing 10% FBS. A 70-μm BD Falcon cell strainer was used to remove the undissociated tissue. Cells were plated in polyethyleneimine-coated 35-mm-diameter dishes at a density of ~100 cells/mm^2 culture surface. Cultures were maintained in Neurobasal medium containing B-27 supplements, 10 units/ml penicillin, 10 μg/ml streptomycin (Life Technologies, Inc.), 2 mM L-glutamine, and 1 mM HEPES (Sigma-Aldrich). All experiments were subsequently performed on healthy primary neuronal cultures after 6–8 days of *in vitro* culture.

Primary neuron calcium imaging

Primary neurons were loaded with 5 μM Fluo-8 AM (TEFLabs, Austin, TX) for 20 min followed by washing three times. Confocal imaging was performed using a Zeiss (Oberkochen, Germany) 710 confocal laser-scanning microscope with a ×40/1.3 oil DIC M27 reverse objective. The 488-nm argon laser line was used to excite Fluo-8 fluorescence, which was measured by a band-pass filter from 493 to 630 nm. The illumination intensity was kept to a minimum (at 2.0% of laser output) to avoid photobleaching, and the pinhole was set to give an optical slice of 3 μm. Glutamate was added to generate a final concentration of 100 μM after an 80-s baseline recording period. A 5-min time series of fluorescence images was recorded. Images of Fluo-8 fluorescence intensities were collected every 2 s. The fluorescence intensity presented was normalized with respect to time zero, calculated by $\Delta F/F = (F - F_{base})/(F_{base} - B)$. The experiment was repeated multiple times ($n = 4$), and 20 representative cells from each group were chosen to perform the statistical analysis.

RNA extraction and microarray analysis

For microarray analysis of transcriptomic expression patterns in murine CNS tissues, specific, dissected brain regions were first homogenized using a Beadbeater (Biospec, Bartlesville, OK) followed by RNA purification using the RNEasy Mini Kit (Qiagen) according to the manufacturer's instructions. The RNA was examined for quantity and quality using an Agilent Bioanalyzer 2100 (Agilent Technologies, Palo Alto, CA). Total RNA was used to generate biotin-labeled cRNA using an Illumina TotalPrep RNA amplification kit (Ambion, Austin, TX). A total of 0.75 μg of biotin-labeled cRNA was hybridized at 58 °C for 16 h to the Illumina Sentrix Mouse Ref-8 Expression BeadChip kit (Illumina, San Diego, CA). The microarrays were then washed and blocked, and the labeled cRNA was detected by staining with streptavidin-Cy3. The arrays were scanned using an Illumina BeadStation ×500 genetic analysis systems scanner, and the image data were extracted using Illumina BeadStudio software, version 3.0. We deposited the raw transcriptomic data at GEO/ArrayExpress under accession number GSE97677. All experimental details are MIAME (minimum information about a microarray experiment)-compliant.

Real-time PCR

For each experimental sample, 1 μg of total RNA was used to synthesize first-strand cDNA using the Invitrogen SuperScript® III first-strand synthesis kit. Semiquantitative real-time PCR was performed using SABiosciences RT^2 qPCR master mix. The real-time primers used were: 5′-ATGTGGTGCACTCCAAAA-3′ and 5′-TAAGCTCCCCTTCTGAAGCA-3′ for Tmem87a; 5′-AAGCTGACGGAGCTGATGTT-3′ and 5′-TTGACGATGCCTTGCTGTAG-3′ for Actl6b; 5′-CTGGGTCGACGAGAAGACTC-3′ and 5′-GCTCCAATACGGTCGATGTT-3′ for Taf6; 5′-GTATTCCAAATGGGGCAATG-3′ and 5′-CACGTAGCCGACAGAGATGA-3′ for H2-B1; 5′-ATGTGCAAACCCTGAGGAAG-3′ and 5′-TCCTCTTGAGGGCTGTGTCT-3′ for Cc121a; 5′-GCAGATGGGTGCTATCCT-3′ and 5′-GCTTTCTTGGCATTCCTT-3′ for T1R3; and 5′-TGTTACCAACTGGGACGACA-3′ and 5′-AAGGAAGGCTGGAAAAGAGC-3′ for β-actin. β-Actin was used as an endogenous housekeeping reference. A non-paired two-way Student's t test was applied using GraphPad Prism, v. 5.0. Statistical significance was considered from $p \leq 0.001$ to ≤ 0.05.

iTRAQ quantitative proteomics

Isobaric tags for relative and absolute quantification (iTRAQ)-based proteomics was performed as described previously (170). iTRAQ labeling reagents were obtained from Applied Biosystems (Carlsbad, CA). WT and T1R3KO tissue samples (150 μg of initial total protein from each animal) were treated in parallel throughout the iTRAQ labeling procedure. Post-labeling WT control and T1R3KO peptide samples (for a single specific tissue) were combined and dried down to a volume of 50 μl to reduce the content of ethanol prior to strong cation exchange chromatography, which was performed as described previously (171); the labeled samples were introduced by nanospray mass spectrometry.

Mass spectrometry analysis

An Eksigent NanoLC Ultra 2D system (Dublin, CA) and a Thermo Fisher Scientific LTQ Orbitrap XL mass spectrometer were used for quantitative proteomic analysis. Tandem liquid chromatography-mass spectrometric analyses were performed as described previously (47). For iTRAQ quantification, the reporter ion intensities in MS2 spectra from raw data sets were used to calculate the expression ratios between the contrasting states. iTRAQ data were analyzed using DIANE 6.0, a spreadsheet-based microarray analysis program based on the SAS

JMP7.0 system. Raw iTRAQ data, subjected to filtering and Z-normalization, were tested for significant changes as described previously (163). Briefly, sample quality was analyzed by scatter plot and protein sample Z-score-based hierarchical clustering to exclude possible outliers. The initial filtering identified proteins with a Z-ratio ≥ 1.20, with the Z-ratio derived from the difference between the averages of the observed protein Z-scores divided by the standard deviation of all of the differences for that particular comparison. We were able to detect ~200 proteins after filtering. Proteins were then refined by calculating the false discovery rate (FDR), which controls for the expected proportion of falsely rejected hypotheses, and including only those proteins with FDR < 0.05. These data were further analyzed using a one-way analysis-of-variance design with significance set at $p < 0.05$. The analysis-of-variance design was compared between the T1R3KO and WT groups. This allowed us to identify proteins that differed in their expression for T1R3KO compared with the WT controls.

Bioinformatic analyses

After identifying significantly altered proteins using iTRAQ, the protein sets were analyzed using a multidimensional bioinformatic approach. To facilitate the specific separation of complex data sets, we employed the novel Venn diagram platform, VennPlex (172). IPA was employed for canonical signaling pathway enrichment as well as biofunction/disease annotation. For both of these pathway/functional enrichment techniques the same minimum pathway population criteria were applied, *i.e.* ≥ 2 experimental proteins present for each pathway at an enrichment probability of $p \leq 0.05$. In addition to these standard pathway enrichment approaches, we employed our in-house-developed NLP latent semantic indexing-based informatics platform, *Textrous!* (50). *Textrous!* facilitates the creation of highly data-specific *de novo* signaling descriptions, thus generating a more nuanced appreciation of high-dimensionality pathological signaling paradigms (173, 174). Word clouds were generated with Wordle (http://www.wordle.net/)[4] from *Textrous!*-based NLP analyses. To extract both word and phrase frequencies from our *Textrous!* output, we employed the Word Frequency Counter application from WriteWords (http://www.writewords.org.uk/word_count.asp).[4]

Statistical analysis

For statistical analyses, a non-paired two-way Student's *t* test was applied using GraphPad Prism v.5.0. Statistical significance was considered as follows: $p \leq 0.001$ (***); $p \leq 0.01$ (**); and $p \leq 0.05$ (*). Data are presented in Figs. 2–4 and 9–11 as mean ± S.E.

Author contributions—B. M. and S. M. contributed to the conception and design of the study, the supervision, the data acquisition, analysis, and interpretation, the manuscript drafting, and the critical revision of the manuscript. R. W., W. C., C. M. D., W. W. W., B. N., K. G. B., E. L., W. H. W., Y. Z., J. V. G., H. E., A. A., and J. J. contributed to the data acquisition, analysis, and interpretation, the manuscript drafting, and the critical revision of the manuscript. B. M. and R. W. contributed equally to this manuscript. The study was supervised by B. M. and S. M. All authors read and approved the final manuscript.

Acknowledgments—We thank Dr. Charles Zuker (Columbia University) for donating T1R3 KO breeding pairs. We thank Patrice Carr and Dr. Mary Ann Wilson from Johns Hopkins University for Golgi staining assistance and Dr. Fred Indig of the NIA Confocal Imaging Facility, National Institutes of Health, for assistance with cell imaging.

References

1. Shin, Y. K., Martin, B., Golden, E., Dotson, C. D., Maudsley, S., Kim, W., Jang, H. J., Mattson, M. P., Drucker, D. J., Egan, J. M., and Munger, S. D. (2008) Modulation of taste sensitivity by GLP-1 signaling. *J. Neurochem.* **106,** 455–463
2. Martin, B., Shin, Y. K., White, C. M., Ji, S., Kim, W., Carlson, O. D., Napora, J. K., Chadwick, W., Chapter, M., Waschek, J. A., Mattson, M. P., Maudsley, S., and Egan, J. M. (2010) Vasoactive intestinal peptide-null mice demonstrate enhanced sweet taste preference, dysglycemia, and reduced taste bud leptin receptor expression. *Diabetes* **59,** 1143–1152
3. Cai, H., Maudsley, S., and Martin, B. (2014) What is the role of metabolic hormones in taste buds of the tongue. *Front. Horm. Res.* **42,** 134–146
4. Spreckley, E., and Murphy, K. G. (2015) The L-cell in nutritional sensing and the regulation of appetite. *Front. Nutr.* **2,** 23
5. Depoortere, I. (2014) Taste receptors of the gut: Emerging roles in health and disease. *Gut* **63,** 179–190
6. Hamr, S. C., Wang, B., Swartz, T. D., and Duca, F. A. (2015) Does nutrient sensing determine how we "see" food? *Curr. Diab. Rep.* **15,** 604
7. Temussi, P. A. (2002) Why are sweet proteins sweet?: Interaction of brazzein, monellin and thaumatin with the T1R2-T1R3 receptor. *FEBS Lett.* **526,** 1–4
8. Zhao, G. Q., Zhang, Y., Hoon, M. A., Chandrashekar, J., Erlenbach, I., Ryba, N. J., and Zuker, C. S. (2003) The receptors for mammalian sweet and umami taste. *Cell* **115,** 255–266
9. Jiang, P., Ji, Q., Liu, Z., Snyder, L. A., Benard, L. M., Margolskee, R. F., and Max, M. (2004) The cysteine-rich region of T1R3 determines responses to intensely sweet proteins. *J. Biol. Chem.* **279,** 45068–45075
10. Tordoff, M. G., Shao, H., Alarcón, L. K., Margolskee, R. F., Mosinger, B., Bachmanov, A. A., Reed, D. R., and McCaughey, S. (2008) Involvement of T1R3 in calcium-magnesium taste. *Physiol. Genomics* **34,** 338–348
11. San Gabriel, A., Uneyama, H., Maekawa, T., and Torii, K. (2009) The calcium-sensing receptor in taste tissue. *Biochem. Biophys. Res. Commun.* **378,** 414–418
12. Tordoff, M. G., Alarcón, L. K., Valmeki, S., and Jiang, P. (2012) T1R3: A human calcium taste receptor. *Sci. Rep.* **2,** 496
13. Wauson, E. M., Lorente-Rodríguez, A., and Cobb, M. H. (2013) Minireview: Nutrient sensing by G protein-coupled receptors. *Mol. Endocrinol.* **27,** 1188–1197
14. Ren, X., Zhou, L., Terwilliger, R., Newton, S. S., and de Araujo, I. E. (2009) Sweet taste signaling functions as a hypothalamic glucose sensor. *Front. Integr. Neurosci.* **3,** 12
15. Wauson, E. M., Zaganjor, E., Lee, A. Y., Guerra, M. L., Ghosh, A. B., Bookout, A. L., Chambers, C. P., Jivan, A., McGlynn, K., Hutchison, M. R., Deberardinis, R. J., and Cobb, M. H. (2012) The G protein-coupled taste receptor T1R1/T1R3 regulates mTORC1 and autophagy. *Mol. Cell* **47,** 851–862
16. Ménard, C., and Quirion, R. (2012) Group 1 metabotropic glutamate receptor function and its regulation of learning and memory in the aging brain. *Front. Pharmacol.* **3,** 182
17. Talevi, A., Enrique, A. V., and Bruno-Blanch, L. E. (2012) Anticonvulsant activity of artificial sweeteners: A structural link between sweet-taste receptor T1R3 and brain glutamate receptors. *Bioorg. Med. Chem. Lett.* **22,** 4072–4074
18. Goeldner, C., Ballard, T. M., Knoflach, F., Wichmann, J., Gatti, S., and Umbricht, D. (2013) Cognitive impairment in major depression and the mGlu2 receptor as a therapeutic target. *Neuropharmacology* **64,** 337–346

19. Morris, K. A., Chang, Q., Mohler, E. G., and Gold, P. E. (2010) Age-related memory impairments due to reduced blood glucose responses to epinephrine. *Neurobiol. Aging* **31,** 2136–2145
20. Morris, K. A., and Gold, P. E. (2013) Epinephrine and glucose modulate training-related CREB phosphorylation in old rats: Relationships to age-related memory impairments. *Exp. Gerontol.* **48,** 115–127
21. Winocur, G., and Gagnon, S. (1998) Glucose treatment attenuates spatial learning and memory deficits of aged rats on tests of hippocampal function. *Neurobiol. Aging* **19,** 233–241
22. Countryman, R. A., and Gold, P. E. (2007) Rapid forgetting of social transmission of food preferences in aged rats: Relationship to hippocampal CREB activation. *Learn. Mem.* **14,** 350–358
23. McNay, E. C., and Sherwin, R. S. (2004) Effect of recurrent hypoglycemia on spatial cognition and cognitive metabolism in normal and diabetic rats. *Diabetes* **53,** 418–425
24. Wang, R., Ross, C. A., Cai, H., Cong, W. N., Daimon, C. M., Carlson, O. D., Egan, J. M., Siddiqui, S., Maudsley, S., and Martin, B. (2014) Metabolic and hormonal signatures in pre-manifest and manifest Huntington's disease patients. *Front. Physiol.* **5,** 231
25. Cahana-Amitay, D., Spiro, A., 3rd, Cohen, J. A., Oveis, A. C., Ojo, E. A., Sayers, J. T., Obler, L. K., and Albert, M. L. (2015) Effects of metabolic syndrome on language functions in aging. *J. Int. Neuropsychol. Soc.* **21,** 116–125
26. Exalto, L. G., van der Flier, W. M., van Boheemen, C. J., Kappelle, L. J., Vrenken, H., Teunissen, C., Koene, T., Scheltens, P., and Biessels, G. J. (2015) The metabolic syndrome in a memory clinic population: relation with clinical profile and prognosis. *J. Neurol. Sci.* **351,** 18–23
27. Euskirchen, P., Buchert, R., Koch, A., Schulz-Schaeffer, W. J., Schreiber, S. J., and Sobesky, J. (2014) Sporadic Creutzfeldt-Jakob disease with mesiotemporal hypermetabolism. *J. Neurol. Sci.* **345,** 278–280
28. Siervo, M., Harrison, S. L., Jagger, C., Robinson, L., and Stephan, B. C. (2014) Metabolic syndrome and longitudinal changes in cognitive function: A systematic review and meta-analysis. *J. Alzheimers Dis.* **41,** 151–161
29. Lee, S., Tong, M., Hang, S., Deochand, C., and de la Monte, S. (2013) CSF and brain indices of insulin resistance, oxidative stress and neuro-inflammation in early versus late Alzheimer's disease. *J. Alzheimers Dis. Parkinsonism* **3,** 128
30. Green, E., Jacobson, A., Haase, L., and Murphy, C. (2015) Neural correlates of taste and pleasantness evaluation in the metabolic syndrome. *Brain Res.* **1620,** 57–71
31. Bohnen, N. I., Müller, M. L. (2013) In vivo neurochemical imaging of olfactory dysfunction in Parkinson's disease. *J. Neural Transm.* **120,** 571–576
32. Heyanka, D. J., Golden, C. J., McCue, R. B., 2nd, Scarisbrick, D. M., Linck, J. F., and Zlatkin, N. I. (2014) Olfactory deficits in frontotemporal dementia as measured by the Alberta Smell Test. *Appl. Neuropsychol. Adult* **21,** 176–182
33. Barrios, F. A., Gonzalez, L., Favila, R., Alonso, M. E., Salgado, P. M., Diaz, R., and Fernandez-Ruiz, J. (2007) Olfaction and neurodegeneration in HD. *Neuroreport* **18,** 73–76
34. Mohajeri, M. H., and Wolfer, D. P. (2009) Neprilysin deficiency-dependent impairment of cognitive functions in a mouse model of amyloidosis. *Neurochem. Res.* **34,** 717–726
35. Shin, Y. K., Cong, W. N., Cai, H., Kim, W., Maudsley, S., Egan, J. M., and Martin, B. (2012) Age-related changes in mouse taste bud morphology, hormone expression, and taste responsivity. *J. Gerontol. A Biol. Sci. Med. Sci.* **67,** 336–344
36. Martin, B., Maudsley, S., White, C. M., and Egan, J. M. (2009) Hormones in the naso-oropharynx: Endocrine modulation of taste and smell. *Trends Endocrinol. Metab.* **20,** 163–170
37. Woolley, J. D., Gorno-Tempini, M. L., Seeley, W. W., Rankin, K., Lee, S. S., Matthews, B. R., and Miller, B. L. (2007) Binge eating is associated with right orbitofrontal-insular-striatal atrophy in frontotemporal dementia. *Neurology* **69,** 1424–1433
38. Ahmed, R. M., Irish, M., Kam, J., van Keizerswaard, J., Bartley, L., Samaras, K., Hodges, J. R., and Piguet, O. (2014) Quantifying the eating abnormalities in frontotemporal dementia. *JAMA Neurol.* **71,** 1540–1546
39. Piguet, O., Petersén, A., Yin Ka Lam, B., Gabery, S., Murphy, K., Hodges, J. R., and Halliday, G. M. (2011) Eating and hypothalamus changes in behavioral-variant frontotemporal dementia. *Ann. Neurol.* **69,** 312–319
40. Snowden, J. S., Bathgate, D., Varma, A., Blackshaw, A., Gibbons, Z. C., and Neary, D. (2001) Distinct behavioural profiles in frontotemporal dementia and semantic dementia. *J. Neurol. Neurosurg. Psychiatry* **70,** 323–332
41. Verfaillie, S. C., Adriaanse, S. M., Binnewijzend, M. A., Benedictus, M. R., Ossenkoppele, R., Wattjes, M. P., Pijnenburg, Y. A., van der Flier, W. M., Lammertsma, A. A., Kuijer, J. P., Boellaard, R., Scheltens, P., van Berckel, B. N., and Barkhof, F. (2015) Cerebral perfusion and glucose metabolism in Alzheimer's disease and frontotemporal dementia: Two sides of the same coin? *Eur. Radiol.* **25,** 3050–3059
42. Jacova, C., Hsiung, G. Y., Tawankanjanachot, I., Dinelle, K., McCormick, S., Gonzalez, M., Lee, H., Sengdy, P., Bouchard-Kerr, P., Baker, M., Rademakers, R., Sossi, V., Stoessl, A. J., Feldman, H. H., and Mackenzie, I. R. (2013) Anterior brain glucose hypometabolism predates dementia in progranulin mutation carriers. *Neurology* **81,** 1322–1331
43. Laws, S. M., Perneczky, R., Drzezga, A., Diehl-Schmid, J., Ibach, B., Bauml, J., Eisele, T., Forstl, H., Kurz, A., and Riemenschneider, M. (2007) Association of the Tau haplotype H2 with age at onset and functional alterations of glucose utilization in frontotemporal dementia. *A. J. Psychiatry* **164,** 1577–1584
44. Kojima, I., Nakagawa, Y., Ohtsu, Y., Medina, A., and Nagasawa, M. (2014) Sweet taste-sensing receptors expressed in pancreatic beta-cells: Sweet molecules act as biased agonists. *Endocrinol. Metab. (Seoul)* **29,** 12–19
45. Cong, W. N., Cai, H., Wang, R., Daimon, C. M., Maudsley, S., Raber, K., Canneva, F., von Hörsten, S., and Martin, B. (2012) Altered hypothalamic protein expression in a rat model of Huntington's disease. *PLoS One* **7,** e47240
46. Martin, B., Chadwick, W., Cong, W. N., Pantaleo, N., Daimon, C. M., Golden, E. J., Becker, K. G., Wood W. H., 3rd, Carlson, O. D., Egan, J. M., and Maudsley, S. (2012) Euglycemic agent-mediated hypothalamic transcriptomic manipulation in the N171–82Q model of Huntington disease is related to their physiological efficacy. *J. Biol. Chem.* **287,** 31766–31782
47. Daimon, C. M., Jasien, J. M., Wood, W. H., 3rd, Zhang, Y., Becker, K. G., Silverman, J. L., Crawley, J. N., Martin, B., and Maudsley, S. (2015) Hippocampal transcriptomic and proteomic alterations in the BTBR mouse model of autism spectrum disorder. *Front. Physiol.* **6,** 324
48. Martin, B., Chadwick, W., Janssens, J., Premont, R. T., Schmalzigaug, R., Becker, K. G., Lehrmann, E., Wood, W. H., Zhang, Y., Siddiqui, S., Park, S. S., Cong, W. N., Daimon, C. M., and Maudsley, S. (2015) GIT2 acts as a systems-level coordinator of neurometabolic activity and pathophysiological aging. *Front. Endocrinol. (Lausanne)* **6,** 191
49. Chen, H., Martin, B., Daimon, C. M., and Maudsley, S. (2013) Effective use of latent semantic indexing and computational linguistics in biological and biomedical applications. *Front. Physiol.* **4,** 8
50. Chen, H., Martin, B., Daimon, C. M., Siddiqui, S., Luttrell, L. M., and Maudsley, S. (2013) Textrous!: Extracting semantic textual meaning from gene sets. *PLoS One* **8,** e62665
51. Baroukh, C., Jenkins, S. L., Dannenfelser, R., and Ma'ayan, A. (2011) Genes2WordCloud: A quick way to identify biological themes from gene lists and free text. *Source Code Biol. Med.* **6,** 15
52. Cheung, W. A., Ouellette, B. F., and Wasserman, W. W. (2012) Inferring novel gene-disease associations using medical subject heading over-representation profiles. *Genome Med.* **4,** 75
53. Lynch, V. J., Nnamani, M. C., Kapusta, A., Brayer, K., Plaza, S. L., Mazur, E. C., Emera, D., Sheikh, S. Z., Grützner, F., Bauersachs, S., Graf, A., Young, S. L., Lieb, J. D., DeMayo, F. J., Feschotte, C., and Wagner, G. P. (2015) Ancient transposable elements transformed the uterine regulatory landscape and transcriptome during the evolution of mammalian pregnancy. *Cell Rep.* **10,** 551–561
54. Shin, Y. K., Martin, B., Kim, W., White, C. M., Ji, S., Sun, Y., Smith, R. G., Sévigny, J., Tschöp, M. H., Maudsley, S., and Egan, J. M. (2010) Ghrelin is produced in taste cells and ghrelin receptor null mice show reduced taste responsivity to salty (NaCl) and sour (citric acid) tastants. *PLoS One* **5,** e12729

55. Meyer-Gerspach, A. C., Wölnerhanssen, B., and Beglinger, C. (2014) Gut sweet taste receptors and their role in metabolism. *Front. Horm. Res.* **42,** 123–133
56. Kinnamon, S. C. (2012) Taste receptor signalling: From tongues to lungs. *Acta Physiol.* (*Oxf.*) **204,** 158–168
57. Nakagawa, Y., Nagasawa, M., Yamada, S., Hara, A., Mogami, H., Nikolaev, V. O., Lohse, M. J., Shigemura, N., Ninomiya, Y., and Kojima, I. (2009) Sweet taste receptor expressed in pancreatic beta-cells activates the calcium and cyclic AMP signaling systems and stimulates insulin secretion. *PLoS One* **4,** e5106
58. Pedrós, I., Petrov, D., Artiach, G., Abad, S., Ramon-Duaso, C., Sureda, F., Pallàs, M., Beas-Zarate, C., Folch, J., and Camins, A. (2015) Adipokine pathways are altered in hippocampus of an experimental mouse model of Alzheimer's disease. *J. Nutr. Health Aging* **19,** 403–412
59. Riise, J., Plath, N., Pakkenberg, B., and Parachikova, A. (2015) Aberrant Wnt signaling pathway in medial temporal lobe structures of Alzheimer's disease. *J. Neural Transm.* **122,** 1303–1318
60. Song, J. M., Sung, Y. M., Nam, J. H., Yoon, H., Chung, A., Moffat, E., Jung, M., Pak, D. T., Kim, J., and Hoe, H. S. (2016) A mercaptoacetamide-based class II histone deacetylase inhibitor increases dendritic spine density via RasGRF1/ERK pathway. *J. Alzheimers Dis.* **51,** 591–604
61. James, B. D., Wilson, R. S., Boyle, P. A., Trojanowski, J. Q., Bennett, D. A., and Schneider, J. A. (2016) TDP-43 stage, mixed pathologies, and clinical Alzheimer's-type dementia. *Brain* **139,** 2983–2993
62. Davis, S. A., Gan, K. A., Dowell, J. A., Cairns, N. J., and Gitcho, M. A. (2017) TDP-43 expression influences amyloidβ plaque deposition and Tau aggregation. *Neurobiol. Dis.* **103,** 154–162
63. Fivaz, M., and Meyer, T. (2005) Reversible intracellular translocation of KRas but not HRas in hippocampal neurons regulated by Ca2+/calmodulin. *J. Cell Biol.* **170,** 429–441
64. Ransome, M. I., and Turnley, A. M. (2008) Growth hormone signaling and hippocampal neurogenesis: Insights from genetic models. *Hippocampus* **18,** 1034–1050
65. Darcy, M. J., Trouche, S., Jin, S. X., and Feig, L. A. (2014) Age-dependent role for Ras-GRF1 in the late stages of adult neurogenesis in the dentate gyrus. *Hippocampus* **24,** 315–325
66. Mira, H., Andreu, Z., Suh, H., Lie, D. C., Jessberger, S., Consiglio, A., San Emeterio, J., Hortigüela, R., Marqués-Torrejón, M. A., Nakashima, K., Colak, D., Götz, M., Fariñas, I., and Gage, F. H. (2010) Signaling through BMPR-IA regulates quiescence and long-term activity of neural stem cells in the adult hippocampus. *Cell Stem Cell* **7,** 78–89
67. Yun, K., Mantani, A., Garel, S., Rubenstein, J., and Israel, M. A. (2004) Id4 regulates neural progenitor proliferation and differentiation *in vivo*. *Development* **131,** 5441–5448
68. von Bohlen und Halbach, O. (2011) Immunohistological markers for proliferative events, gliogenesis, and neurogenesis within the adult hippocampus. *Cell Tissue Res.* **345,** 1–19
69. Sabater, L., Gómez-Choco, M., Saiz, A., and Graus, F. (2005) BR serine/threonine kinase 2: A new autoantigen in paraneoplastic limbic encephalitis. *J. Neuroimmunol.* **170,** 186–190
70. Rosso, S. B., Sussman, D., Wynshaw-Boris, A., and Salinas, P. C. (2005) Wnt signaling through Dishevelled, Rac, and JNK regulates dendritic development. *Nat. Neurosci.* **8,** 34–42
71. Davis, E. K., Zou, Y., and Ghosh, A. (2008) Wnts acting through canonical and noncanonical signaling pathways exert opposite effects on hippocampal synapse formation. *Neural Dev.* **3,** 32
72. Behnke, J., Cheedalla, A., Bhatt, V., Bhat, M., Teng, S., Palmieri, A., Windon, C. C., Thakker-Varia, S., and Alder, J. (2017) Neuropeptide VGF promotes maturation of hippocampal dendrites that is reduced by single nucleotide polymorphisms. *Int J. Mol. Sci.* **18,** E612
73. Decker, J. M., Wójtowicz, A. M., Bartsch, J. C., Liotta, A., Braunewell, K. H., Heinemann, U., and Behrens, C. J. (2010) C-type natriuretic peptide modulates bidirectional plasticity in hippocampal area CA1 *in vitro*. *Neuroscience* **169,** 8–22
74. Cohen, D., Segal, M., and Reiner, O. (2008) Doublecortin supports the development of dendritic arbors in primary hippocampal neurons. *Dev. Neurosci.* **30,** 187–199
75. Tursun, B., Schlüter, A., Peters, M. A., Viehweger, B., Ostendorff, H. P., Soosairajah, J., Drung, A., Bossenz, M., Johnsen, S. A., Schweizer, M., Bernard, O., and Bach, I. (2005) The ubiquitin ligase Rnf6 regulates local LIM kinase 1 levels in axonal growth cones. *Genes Dev.* **19,** 2307–2319
76. Yamashita, N., Yamane, M., Suto, F., and Goshima, Y. (2016) TrkA mediates retrograde semaphorin 3A signaling through plexin A4 to regulate dendritic branching. *J. Cell Sci.* **129,** 1802–1814
77. Nie, D., Chen, Z., Ebrahimi-Fakhari, D., Di Nardo, A., Julich, K., Robson, V. K., Cheng, Y. C., Woolf, C. J., Heiman, M., and Sahin, M. (2015) The stress-induced Atf3-gelsolin cascade underlies dendritic spine deficits in neuronal models of tuberous sclerosis complex. *J. Neurosci.* **35,** 10762–10772
78. Kim, Y. N., Jung, H. Y., Eum, W. S., Kim, D. W., Shin, M. J., Ahn, E. H., Kim, S. J., Lee, C. H., Yong, J. I., Ryu, E. J., Park, J., Choi, J. H., Hwang, I. K., and Choi, S. Y. (2014) Neuroprotective effects of PEP-1-carbonyl reductase 1 against oxidative-stress-induced ischemic neuronal cell damage. *Free Radic. Biol. Med.* **69,** 181–196
79. Yang, L., Wang, M., Guo, Y. Y., Sun, T., Li, Y. J., Yang, Q., Zhang, K., Liu, S. B., Zhao, M. G., and Wu, Y. M. (2016) Systemic inflammation induces anxiety disorder through CXCL12/CXCR4 pathway. *Brain Behav. Immun.* **56,** 352–362
80. Ehninger, D., and Silva, A. J. (2011) Increased levels of anxiety-related behaviors in a Tsc2 dominant negative transgenic mouse model of tuberous sclerosis. *Behav. Genet.* **41,** 357–363
81. Tomasevic, G., Laurer, H. L., Mattiasson, G., van Steeg, H., Wieloch, T., and McIntosh, T. K. (2012) Delayed neuromotor recovery and increased memory acquisition dysfunction following experimental brain trauma in mice lacking the DNA repair gene *XPA*. *J. Neurosurg.* **116,** 1368–1378
82. Fernández-Medarde, A., Porteros, A., de las Rivas, J., Núñez, A., Fuster, J. J., and Santos, E. (2007) Laser microdissection and microarray analysis of the hippocampus of Ras-GRF1 knockout mice reveals gene expression changes affecting signal transduction pathways related to memory and learning. *Neuroscience* **146,** 272–285
83. Wu, K., Li, S., Bodhinathan, K., Meyers, C., Chen, W., Campbell-Thompson, M., McIntyre, L., Foster, T. C., Muzyczka, N., and Kumar, A. (2012) Enhanced expression of Pctk1, Tcf12 and Ccnd1 in hippocampus of rats: Impact on cognitive function, synaptic plasticity and pathology. *Neurobiol. Learn Mem.* **97,** 69–80
84. Kumar, D., and Thakur, M. K. (2015) Age-related expression of Neurexin1 and Neuroligin3 is correlated with presynaptic density in the cerebral cortex and hippocampus of male mice. *Age (Dordr)* **37,** 17
85. Lee, T. H., Pastorino, L., and Lu, K. P. (2011) Peptidyl-prolyl cis-trans isomerase Pin1 in ageing, cancer, and Alzheimer disease. *Expert Rev. Mol. Med.* **13,** e21
86. Choi, K. J., Kim, M. J., Je, A. R., Jun, S., Lee, C., Lee, E., Jo, M., Huh, Y. H., and Kweon, H. S. (2014) Three-dimensional analysis of abnormal ultrastructural alteration in mitochondria of hippocampus of APP/PSEN1 transgenic mouse. *J. Biosci.* **39,** 97–105
87. Potkin, S. G., Turner, J. A., Fallon, J. A., Lakatos, A., Keator, D. B., Guffanti, G., and Macciardi, F. (2009) Gene discovery through imaging genetics: Identification of two novel genes associated with schizophrenia. *Mol. Psychiatry* **14,** 416–428
88. Fukai, R., Hiraki, Y., Nishimura, G., Nakashima, M., Tsurusaki, Y., Saitsu, H., Matsumoto, N., and Miyake, N. (2014) A *de novo* 1.4-Mb deletion at 21q22.11 in a boy with developmental delay. *Am. J. Med. Genet. A* **164A,** 1021–1028
89. Lai, J. K., Doering, L. C., and Foster, J. A. (2016) Developmental expression of the neuroligins and neurexins in fragile X mice. *J. Comp. Neurol.* **524,** 807–828
90. Heese, K., Yamada, T., Akatsu, H., Yamamoto, T., Kosaka, K., Nagai, Y., and Sawada, T. (2004) Characterizing the new transcription regulator protein p60TRP. *J. Cell. Biochem.* **91,** 1030–1042
91. Miura, Y., Sakurai, Y., and Endo, T. (2012) O-GlcNAc modification affects the ATM-mediated DNA damage response. *Biochim. Biophys. Acta* **1820,** 1678–1685
92. Terry, R. D., Masliah, E., Salmon, D. P., Butters, N., DeTeresa, R., Hill, R., Hansen, L. A., and Katzman, R. (1991) Physical basis of cognitive altera-

tions in Alzheimer's disease: Synapse loss is the major correlate of cognitive impairment. *Ann. Neurol.* **30,** 572–580
93. Bittner, T., Fuhrmann, M., Burgold, S., Ochs, S. M., Hoffmann, N., Mitteregger, G., Kretzschmar, H., LaFerla, F. M., and Herms, J. (2010) Multiple events lead to dendritic spine loss in triple transgenic Alzheimer's disease mice. *Plos One* **5,** e15477
94. Richards, P., Didszun, C., Campesan, S., Simpson, A., Horley, B., Young, K. W., Glynn, P., Cain, K., Kyriacou, C. P., Giorgini, F., and Nicotera, P. (2011) Dendritic spine loss and neurodegeneration is rescued by Rab11 in models of Huntington's disease. *Cell Death Differ.* **18,** 191–200
95. Yasuda, R. (2012) Studying signal transduction in single dendritic spines. *Cold Spring Harb. Perspect. Biol.* **4,** a005611
96. Nimchinsky, E. A., Sabatini, B. L., and Svoboda, K. (2002) Structure and function of dendritic spines. *Annu. Rev. Physiol.* **64,** 313–353
97. Alvarez, V. A., and Sabatini, B. L. (2007) Anatomical and physiological plasticity of dendritic spines. *Annu. Rev. Neurosci.* **30,** 79–97
98. Bliss, T. V., and Collingridge, G. L. (1993) A synaptic model of memory: Long-term potentiation in the hippocampus. *Nature* **361,** 31–39
99. Kessels, H. W., and Malinow, R. (2009) Synaptic AMPA receptor plasticity and behavior. *Neuron* **61,** 340–350
100. Derkach, V. A., Oh, M. C., Guire, E. S., and Soderling, T. R. (2007) Regulatory mechanisms of AMPA receptors in synaptic plasticity. *Nat. Rev. Neurosci.* **8,** 101–113
101. Yuste, R., and Denk, W. (1995) Dendritic spines as basic functional units of neuronal integration. *Nature* **375,** 682–684
102. Matsuzaki, M., Honkura, N., Ellis-Davies, G. C., and Kasai, H. (2004) Structural basis of long-term potentiation in single dendritic spines. *Nature* **429,** 761–766
103. Stranahan, A. M., Lee, K., Martin, B., Maudsley, S., Golden, E., Cutler, R. G., and Mattson, M. P. (2009) Voluntary exercise and caloric restriction enhance hippocampal dendritic spine density and BDNF levels in diabetic mice. *Hippocampus* **19,** 951–961
104. Okabe, S., Kim, H. D., Miwa, A., Kuriu, T., and Okado, H. (1999) Continual remodeling of postsynaptic density and its regulation by synaptic activity. *Nat. Neurosci.* **2,** 804–811
105. Bonanomi, D., Menegon, A., Miccio, A., Ferrari, G., Corradi, A., Kao, H. T., Benfenati, F., and Valtorta, F. (2005) Phosphorylation of synapsin I by cAMP-dependent protein kinase controls synaptic vesicle dynamics in developing neurons. *J. Neurosci.* **25,** 7299–7308
106. Rosahl, T. W., Geppert, M., Spillane, D., Herz, J., Hammer, R. E., Malenka, R. C., and Südhof, T. C. (1993) Short-term synaptic plasticity is altered in mice lacking synapsin I. *Cell* **75,** 661–670
107. Allen, P. B., Zachariou, V., Svenningsson, P., Lepore, A. C., Centonze, D., Costa, C., Rossi, S., Bender, G., Chen, G., Feng, J., Snyder, G. L., Bernardi, G., Nestler, E. J., Yan, Z., Calabresi, P., and Greengard, P. (2006) Distinct roles for spinophilin and neurabin in dopamine-mediated plasticity. *Neuroscience* **140,** 897–911
108. Feng, J., Yan, Z., Ferreira, A., Tomizawa, K., Liauw, J. A., Zhuo, M., Allen, P. B., Ouimet, C. C., and Greengard, P. (2000) Spinophilin regulates the formation and function of dendritic spines. *Proc. Natl. Acad. Sci. U.S.A.* **97,** 9287–9292
109. Xu, W. (2011) PSD-95-like membrane associated guanylate kinases (PSD-MAGUKs) and synaptic plasticity. *Curr. Opin. Neurobiol.* **21,** 306–312
110. Elizalde, N., Pastor, P. M., Garcia-García, A. L., Serres, F., Venzala, E., Huarte, J., Ramírez, M. J., Del Rio, J., Sharp, T., and Tordera, R. M. (2010) Regulation of markers of synaptic function in mouse models of depression: Chronic mild stress and decreased expression of VGLUT1. *J. Neurochem.* **114,** 1302–1314
111. Migaud, M., Charlesworth, P., Dempster, M., Webster, L. C., Watabe, A. M., Makhinson, M., He, Y., Ramsay, M. F., Morris, R. G., Morrison, J. H., O'Dell, T. J., and Grant, S. G. (1998) Enhanced long-term potentiation and impaired learning in mice with mutant postsynaptic density-95 protein. *Nature* **396,** 433–439
112. Yuki, D., Sugiura, Y., Zaima, N., Akatsu, H., Takei, S., Yao, I., Maesako, M., Kinoshita, A., Yamamoto, T., Kon, R., Sugiyama, K., and Setou, M. (2014) DHA-PC and PSD-95 decrease after loss of synaptophysin and before neuronal loss in patients with Alzheimer's disease. *Sci. Rep.* **4,** 7130
113. Counts, S. E., Alldred, M. J., Che, S., Ginsberg, S. D., and Mufson, E. J. (2014) Synaptic gene dysregulation within hippocampal CA1 pyramidal neurons in mild cognitive impairment. *Neuropharmacology* **79,** 172–179
114. Warmus, B. A., Sekar, D. R., McCutchen, E., Schellenberg, G. D., Roberts, R. C., McMahon, L. L., and Roberson, E. D. (2014) Tau-mediated NMDA receptor impairment underlies dysfunction of a selectively vulnerable network in a mouse model of frontotemporal dementia. *J. Neurosci.* **34,** 16482–16495
115. Murmu, R. P., Li, W., Szepesi, Z., and Li, J. Y. (2015) Altered sensory experience exacerbates stable dendritic spine and synapse loss in a mouse model of Huntington's disease. *J. Neurosci.* **35,** 287–298
116. Lin, N., Pan, X. D., Chen, A. Q., Zhu, Y. G., Wu, M., Zhang, J., and Chen, X. C. (2014) Tripchlorolide improves age-associated cognitive deficits by reversing hippocampal synaptic plasticity impairment and NMDA receptor dysfunction in SAMP8 mice. *Behav. Brain Res.* **258,** 8–18
117. Meng, C., He, Z., and Xing, D. (2013) Low-level laser therapy rescues dendrite atrophy via upregulating BDNF expression: Implications for Alzheimer's disease. *J. Neurosci.* **33,** 13505–13517
118. Perez-Cruz, C., Nolte, M. W., van Gaalen, M. M., Rustay, N. R., Termont, A., Tanghe, A., Kirchhoff, F., and Ebert, U. (2011) Reduced spine density in specific regions of CA1 pyramidal neurons in two transgenic mouse models of Alzheimer's disease. *J. Neurosci.* **31,** 3926–3934
119. Auffret, A., Gautheron, V., Repici, M., Kraftsik, R., Mount, H. T., Mariani, J., and Rovira, C. (2009) Age-dependent impairment of spine morphology and synaptic plasticity in hippocampal CA1 neurons of a presenilin 1 transgenic mouse model of Alzheimer's disease. *J. Neurosci.* **29,** 10144–10152
120. del Valle, J., Bayod, S., Camins, A., Beas-Zárate, C., Velázquez-Zamora, D. A., González-Burgos, I., and Pallàs, M. (2012) Dendritic spine abnormalities in hippocampal CA1 pyramidal neurons underlying memory deficits in the SAMP8 mouse model of Alzheimer's disease. *J. Alzheimers Dis.* **32,** 233–240
121. Akram, A., Christoffel, D., Rocher, A. B., Bouras, C., Kövari, E., Perl, D. P., Morrison, J. H., Herrmann, F. R., Haroutunian, V., Giannakopoulos, P., and Hof, P. R. (2008) Stereologic estimates of total spinophilin-immunoreactive spine number in area 9 and the CA1 field: Relationship with the progression of Alzheimer's disease. *Neurobiol. Aging* **29,** 1296–1307
122. Rodriguez, G. A., Burns, M. P., Weeber, E. J., and Rebeck, G. W. (2013) Young APOE4 targeted replacement mice exhibit poor spatial learning and memory, with reduced dendritic spine density in the medial entorhinal cortex. *Learn. Mem.* **20,** 256–266
123. Colombari, E., and Talman, W. T. (1995) Denervation supersensitivity to glutamate in the nucleus-tractus-solitarii after removal of the nodose ganglion. *Brain Res.* **677,** 110–116
124. Pivovarova, N. B., and Andrews, S. B. (2010) Calcium-dependent mitochondrial function and dysfunction in neurons. *FEBS J.* **277,** 3622–3636
125. Melachroinou, K., Xilouri, M., Emmanouilidou, E., Masgrau, R., Papazafiri, P., Stefanis, L., and Vekrellis, K. (2013) Deregulation of calcium homeostasis mediates secreted α-synuclein-induced neurotoxicity. *Neurobiol. Aging* **34,** 2853–2865
126. Chadwick, W., Zhou, Y., Park, S. S., Wang, L., Mitchell, N., Stone, M. D., Becker, K. G., Martin, B., and Maudsley, S. (2010) Minimal peroxide exposure of neuronal cells induces multifaceted adaptive responses. *PloS One* **5,** e14352
127. Rex, C. S., Lin, C. Y., Kramár, E. A., Chen, L. Y., Gall, C. M., and Lynch, G. (2007) Brain-derived neurotrophic factor promotes long-term potentiation-related cytoskeletal changes in adult hippocampus. *J. Neurosci.* **27,** 3017–3029
128. Sheng, M., McFadden, G., and Greenberg, M. E. (1990) Membrane depolarization and calcium induce c-*fos* transcription via phosphorylation of transcription factor CREB. *Neuron* **4,** 571–582
129. Molteni, R., Barnard, R. J., Ying, Z., Roberts, C. K., and Gómez-Pinilla, F. (2002) A high-fat, refined sugar diet reduces hippocampal brain-derived neurotrophic factor, neuronal plasticity, and learning. *Neuroscience* **112,** 803–814
130. Bito, H., Deisseroth, K., and Tsien, R. W. (1996) CREB phosphorylation and dephosphorylation: A Ca2(+)- and stimulus duration-dependent switch for hippocampal gene expression. *Cell* **87,** 1203–1214

131. Mizuno, M., Yamada, K., Maekawa, N., Saito, K., Seishima, M., and Nabeshima, T. (2002) CREB phosphorylation as a molecular marker of memory processing in the hippocampus for spatial learning. *Behav. Brain Res.* **133,** 135–141
132. Prasad, S., and Singh, K. (2008) Interaction of USF1/USF2 and alpha-Pal/Nrf1 to Fmr-1 promoter increases in mouse brain during aging. *Biochem. Biophys. Res. Commun.* **376,** 347–351
133. Tran, P. V., Kennedy, B. C., Lien, Y. C., Simmons, R. A., and Georgieff, M. K. (2015) Fetal iron deficiency induces chromatin remodeling at the *Bdnf* locus in adult rat hippocampus. *Am. J. Physiol. Regul. Integr. Comp. Physiol.* **308,** R276–R282
134. Teich, A. F., Nicholls, R. E., Puzzo, D., Fiorito, J., Purgatorio, R., Fa', M., and Arancio, O. (2015) Synaptic therapy in Alzheimer's disease: A CREB-centric approach. *Neurotherapeutics* **12,** 29–41
135. Jaramillo, T. C., Liu, S., Pettersen, A., Birnbaum, S. G., and Powell, C. M. (2014) Autism-related neuroligin-3 mutation alters social behavior and spatial learning. *Autism Research* **7,** 264–272
136. Boccuto, L., Lauri, M., Sarasua, S. M., Skinner, C. D., Buccella, D., Dwivedi, A., Orteschi, D., Collins, J. S., Zollino, M., Visconti, P., Dupont, B., Tiziano, D., Schroer, R. J., Neri, G., Stevenson, R. E., *et al.* (2013) Prevalence of SHANK3 variants in patients with different subtypes of autism spectrum disorders. *Eur. J. Hum. Genet.* **21,** 310–316
137. Rubenstein, J. L., and Merzenich, M. M. (2003) Model of autism: Increased ratio of excitation/inhibition in key neural systems. *Genes Brain Behav.* **2,** 255–267
138. Overk, C. R., and Masliah, E. (2014) Pathogenesis of synaptic degeneration in Alzheimer's disease and Lewy body disease. *Biochem. Pharmacol.* **88,** 508–516
139. Huey, E. D., Putnam, K. T., and Grafman, J. (2006) A systematic review of neurotransmitter deficits and treatments in frontotemporal dementia. *Neurology* **66,** 17–22
140. Hotokezaka, Y., Katayama, I., van Leyen, K., and Nakamura, T. (2015) GSK-3β-dependent downregulation of γ-taxilin and αNAC merge to regulate ER stress responses. *Cell Death Dis.* **6,** e1719
141. Pastorino, L., Sun, A., Lu, P. J., Zhou, X. Z., Balastik, M., Finn, G., Wulf, G., Lim, J., Li, S. H., Li, X., Xia, W., Nicholson, L. K., and Lu, K. P. (2006) The prolyl isomerase Pin1 regulates amyloid precursor protein processing and amyloid-β production. *Nature* **440,** 528–534
142. Butterfield, D. A., Gnjec, A., Poon, H. F., Castegna, A., Pierce, W. M., Klein, J. B., and Martins, R. N. (2006) Redox proteomics identification of oxidatively modified brain proteins in inherited Alzheimer's disease: An initial assessment. *J. Alzheimers Dis.* **10,** 391–397
143. Maudsley, S., and Mattson, M. P. (2006) Protein twists and turns in Alzheimer disease. *Nat. Med.* **12,** 392–393
144. Terwel, D., Lasrado, R., Snauwaert, J., Vandeweert, E., Van Haesendonck, C., Borghgraef, P., and Van Leuven, F. (2005) Changed conformation of mutant Tau-P301L underlies the moribund tauopathy, absent in progressive, nonlethal axonopathy of Tau-4R/2N transgenic mice. *J. Biol. Chem.* **280,** 3963–3973
145. Lim, J., Balastik, M., Lee, T. H., Nakamura, K., Liou, Y. C., Sun, A., Finn, G., Pastorino, L., Lee, V. M., and Lu, K. P. (2008) Pin1 has opposite effects on wild-type and P301L tau stability and tauopathy. *J. Clin. Invest.* **118,** 1877–1889
146. Seltman, R. E., and Matthews, B. R. (2012) Frontotemporal lobar degeneration: Epidemiology, pathology, diagnosis and management. *CNS Drugs* **26,** 841–870
147. Nagaoka, S., Arai, H., Iwamoto, N., Ohwada, J., Ichimiya, Y., Nakamura, M., and Inoue, R. (1995) A juvenile case of frontotemporal dementia: neurochemical and neuropathological investigations. *Prog. Neuropsychopharmacol. Biol. Psychiatry* **19,** 1251–1261
148. Sperfeld, A. D., Collatz, M. B., Baier, H., Palmbach, M., Storch, A., Schwarz, J., Tatsch, K., Reske, S., Joosse, M., Heutink, P., and Ludolph, A. C. (1999) FTDP-17: An early-onset phenotype with parkinsonism and epileptic seizures caused by a novel mutation. *Ann. Neurol.* **46,** 708–715
149. Rinne, J. O., Laine, M., Kaasinen, V., Norvasuo-Heilä, M. K., Någren, K., and Helenius, H. (2002) Striatal dopamine transporter and extrapyramidal symptoms in frontotemporal dementia. *Neurology* **58,** 1489–1493
150. Knecht, S., Breitenstein, C., Bushuven, S., Wailke, S., Kamping, S., Flöel, A., Zwitserlood, P., and Ringelstein, E. B. (2004) Levodopa: Faster and better word learning in normal humans. *Ann. Neurol.* **56,** 20–26
151. Copland, D., Campbell, A., Rawlings, A., McMahon, K., Silburn, P., and Nathan, P. (2015) L-Dopa improves learning and maintenance of new nouns in healthy adults. *Front. Hum. Neurosci. Conference Abstract: XII International Conference on Cognitive Neuroscience (ICON-XII)* 10.3389/conf.fnhum.2015.217.00165
152. Iqbal, Z., Willemsen, M. H., Papon, M. A., Musante, L., Benevento, M., Hu, H., Venselaar, H., Wissink-Lindhout, W. M., Vulto-van Silfhout, A. T., Vissers, L. E., de Brouwer, A. P., Marouillat, S., Wienker, T. F., Ropers, H. H., Kahrizi, K., *et al.* (2015) Homozygous SLC6A17 mutations cause autosomal-recessive intellectual disability with progressive tremor, speech impairment, and behavioral problems. *Am. J. Hum. Genet.* **96,** 386–396
153. Waltl, S. (2015) Mutations in SLC6A17 cause autosomal-recessive intellectual disability. *Clin. Genet.* **88,** 136–137
154. Wagner, M. J., Kim, T. H., Savall, J., Schnitzer, M. J., and Luo, L. (2017) Cerebellar granule cells encode the expectation of reward. *Nature* **544,** 96–100
155. Stoodley, C. J., Valera, E. M., and Schmahmann, J. D. (2012) Functional topography of the cerebellum for motor and cognitive tasks: An fMRI study. *Neuroimage* **59,** 1560–1570
156. Strick, P. L., Dum, R. P., and Fiez, J. A. (2009) Cerebellum and nonmotor function. *Annu. Rev. Neurosci.* **32,** 413–434
157. Ito, M. (2008) Control of mental activities by internal models in the cerebellum. *Nat. Rev. Neurosci.* **9,** 304–313
158. Tsai, P. T., Hull, C., Chu, Y., Greene-Colozzi, E., Sadowski, A. R., Leech, J. M., Steinberg, J., Crawley, J. N., Regehr, W. G., and Sahin, M. (2012) Autistic-like behaviour and cerebellar dysfunction in Purkinje cell Tsc1 mutant mice. *Nature* **488,** 647–651
159. Lauvin, M. A., Martineau, J., Destrieux, C., Andersson, F., Bonnet-Brilhault, F., Gomot, M., El-Hage, W., and Cottier, J. P. (2012) Functional morphological imaging of autism spectrum disorders: Current position and theories proposed. *Diagn. Interv. Imaging* **93,** 139–147
160. Dang, Y. H., Liu, P., Ma, R., Chu, Z., Liu, Y. P., Wang, J. B., Ma, X. C., and Gao, C. G. (2015) HINT1 is involved in the behavioral abnormalities induced by social isolation rearing. *Neurosci. Lett.* **607,** 40–45
161. Varadarajulu, J., Lebar, M., Krishnamoorthy, G., Habelt, S., Lu, J., Bernard Weinstein, I., Li, H., Holsboer, F., Turck, C. W., and Touma, C. (2011) Increased anxiety-related behaviour in Hint1 knockout mice. *Behav. Brain Res.* **220,** 305–311
162. Borroto-Escuela, D. O., Carlsson, J., Ambrogini, P., Narváez, M., Wydra, K., Tarakanov, A. O., Li, X., Millón, C., Ferraro, L., Cuppini, R., Tanganelli, S., Liu, F., Filip, M., Diaz-Cabiale, Z., and Fuxe, K. (2017) Understanding the role of GPCR heteroreceptor complexes in modulating the brain networks in health and disease. *Front. Cell. Neurosci.* **11,** 37
163. Chadwick, W., Mitchell, N., Caroll, J., Zhou, Y., Park, S. S., Wang, L., Becker, K. G., Zhang, Y., Lehrmann, E., Wood, W. H., 3rd, Martin, B., and Maudsley, S. (2011) Amitriptyline-mediated cognitive enhancement in aged 3xTg Alzheimer's disease mice is associated with neurogenesis and neurotrophic activity. *PLoS One* **6,** e21660
164. Cong, W. N., Wang, R., Cai, H., Daimon, C. M., Scheibye-Knudsen, M., Bohr, V. A., Turkin, R., Wood, W. H., 3rd, Becker, K. G., Moaddel, R., Maudsley, S., and Martin, B. (2013) Long-term artificial sweetener acesulfame potassium treatment alters neurometabolic functions in C57BL/6J mice. *PLoS One* **8,** e70257
165. Yang, M., Zhodzishsky, V., and Crawley, J. N. (2007) Social deficits in BTBR T+tf/J mice are unchanged by cross-fostering with C57BL/6J mothers. *Int. J. Dev. Neurosci.* **25,** 515–521
166. Boughter, J. D., Jr., St John, S. J., Noel, D. T., Ndubuizu, O., and Smith, D. V. (2002) A brief-access test for bitter taste in mice. *Chem. Senses* **27,** 133–142
167. Glendinning, J. I., Gresack, J., and Spector, A. C. (2002) A high-throughput screening procedure for identifying mice with aberrant taste and oromotor function. *Chem. Senses* **27,** 461–474
168. Nelson, T. M., Munger, S. D., and Boughter, J. D., Jr. (2003) Taste sensitivities to PROP and PTC vary independently in mice. *Chem. Senses* **28,** 695–704

169. Dotson, C. D., and Spector, A. C. (2004) The relative affective potency of glycine, L-Serine and sucrose as assessed by a brief-access taste test in inbred strains of mice. *Chem. Senses* **29,** 489–498
170. Wu, W. W., Wang, G., Insel, P. A., Hsiao, C. T., Zou, S., Martin, B., Maudsley, S., and Shen, R. F. (2012) Discovery- and target-based protein quantification using iTRAQ and pulsed Q collision-induced dissociation (PQD). *J. Proteomics* **75,** 2480–2487
171. Martin, B., Brenneman, R., Becker, K. G., Gucek, M., Cole, R. N., and Maudsley, S. (2008) iTRAQ analysis of complex proteome alterations in 3xTgAD Alzheimer's mice: Understanding the interface between physiology and disease. *PLoS One* **3,** e2750
172. Cai, H., Chen, H., Yi, T., Daimon, C. M., Boyle, J. P., Peers, C., Maudsley, S., and Martin, B. (2013) VennPlex: A novel Venn diagram program for comparing and visualizing datasets with differentially regulated datapoints. *PLoS One* **8,** e53388
173. Janssens, J., Philtjens, S., Kleinberger, G., Van Mossevelde, S., van der Zee, J., Cacace, R., Engelborghs, S., Sieben, A., Banzhaf-Strathmann, J., Dillen, L., Merlin, C., Cuijt, I., Robberecht, C., Schmid, B., Santens, P., *et al.* (2015) Investigating the role of filamin C in Belgian patients with frontotemporal dementia linked to GRN deficiency in FTLD-TDP brains. *Acta Neuropathol. Commun.* **3,** 68
174. Maudsley, S., Martin, B., Janssens, J., Etienne, H., Jushaj, A., van Gastel, J., Willemsen, A., Chen, H., Gesty-Palmer, D., and Luttrell, L. M. (2016) Informatic deconvolution of biased GPCR signaling mechanisms from *in vivo* pharmacological experimentation. *Methods* **92,** 51–63